



Article

ACAT1 Benchmark of RANS-informed Analytical Methods for Fan Broadband Noise Prediction: Part II - Influence of the Acoustic Models

Sébastien Guérin ^{1*} , Carolin Kissner ¹ , Pascal Seeler ¹, Ricardo Blázquez ², Pedro Carrasco Laraña ³, Hélène de Laborderie ⁴, Danny Lewis ⁵, Paruchuri Chaitanya ⁶, Cyril Polacsek ⁷, and Johan Thisse ⁸

¹ German Aerospace Center (DLR), Institute of Propulsion Technology, Department of Engine Acoustics, Berlin, Germany

² Universidad Politécnica de Madrid (UPM), Department of Engine Propulsion and Fluid Dynamics, Madrid, Spain

³ ITP Aero, Aerodynamic Technology Department, Alcobendas, Spain

⁴ Safran Aircraft Engines, Aerodynamics and Acoustics Department, Moissy Cramayel, France

⁵ Univ. Lyon, Ecole Centrale de Lyon, INSA Lyon, Université Claude Bernard Lyon I, CNRS, Laboratoire de Mécanique des Fluides et d'Acoustique, UMR 5509, Ecully, France

⁶ University of Southampton, Institute of Sound and Vibration Research, Southampton, United Kingdom

⁷ ONERA - The French Aerospace Lab, Department of Aerodynamics, Aeroelasticity, and Acoustics, Châtillon, France

⁸ Airbus Commercial Aircraft, Acoustics Methods, Toulouse, France

* Correspondence: Sebastien.Guerin@dlr.de; Tel.: +49 30 310006-55

Version June 19, 2020 submitted to Acoustics

Abstract: A benchmark dedicated to RANS-informed analytical methods for the prediction of turbofan rotor–stator interaction broadband noise was organised within the framework of the European project TurboNoiseBB. The second part of this benchmark focuses on the impact of the acoustic models. Twelve different approaches implemented in seven different acoustic solvers are compared. Some of the methods resort to the acoustic analogy, while some use a direct approach bypassing the calculation of a source term. Due to differing application objectives, the studied methods vary in terms of fidelity to represent the turbulence, to calculate the acoustic response of the stator, to propagate the acoustic waves, etc. This diversity of approaches constitutes the unique quality of this work. The overall agreement of the predicted sound power spectra is satisfactory. While the low frequency results show greater deviations as they are strongly impacted by the low number of contributing cut-on waves, the levels vary within an interval of ± 3 dB at mid and high frequencies. The trends predicted by increasing the rotor speed are similar for almost all models. However, most predicted levels are some decibels lower than the experimental results.

Keywords: RANS-informed noise prediction; fan broadband noise; ACAT1 fan benchmark

1. Introduction

Research and development activities regarding the design of turbomachinery components of commercial aero-engines call for reliable and efficient methods to predict the noise emission. Hybrid RANS-informed analytical methods can help to reach that objective. RANS simulations are indeed powerful methods, which are standardly applied in the field of engineering. A dedicated post-processing of the RANS results can be applied to reconstruct the input needed by analytical models of fan noise. Thus, if the method works, an acoustic prediction could be achieved as a

22 by-product of a RANS simulation. However two main questions arise regarding that approach: i) Is
 23 RANS able to properly predict the input for the acoustic models, in particular the crucial turbulence
 24 statistics needed for broadband noise prediction? ii) Are analytical models, which tend to strongly
 25 simplify reality, sensitive enough to capture the effects of the sough-after design modifications.

26 The benchmark organised as part of the European project TurboNoiseBB is a contribution to the
 27 assessment of RANS-informed analytical methods applied to rotor–stator interaction (RSI) broadband
 28 noise. While a first part reported in the companion paper by Kissner et al. [1] focuses on the effect of
 29 the RANS model, the present work focuses on the impact of the acoustic model.

30 For several reasons, the low-pressure compressor of an aero-engine, the so-called fan, is the ideal
 31 candidate for testing RANS-informed analytical approaches for turbomachines. Firstly, it is composed
 32 of a single rotor–stator stage unlike high-pressure compressors or turbines, which combine several
 33 blade rows interacting in a very complex manner. Secondly, blades have a high-aspect ratio; this
 34 minimises the contribution of endwall effects, which are difficult to predict. Thirdly, because the
 35 duct contours are slowly varying and the mean flow is predominantly axial, weakly sheared and
 36 moderately swirling, the sound propagation can be reasonably approximated by analytical models,
 37 whose complexity can be increased for more accurate results [2]. Finally, contrary to turbine blades, the
 38 airfoils of transonic fan stages are thin and only slightly cambered, which are favourable conditions
 39 when using the flat plate (zero camber and zero thickness) hypothesis. Specifically, rotor–stator
 40 interaction broadband noise occurs in subsonic conditions so that turbulence–shock noise [3] does
 41 not have to be considered. Furthermore, the stochastic nature of turbulence is expected to make RSI
 42 broadband noise well suited for analytical modelling.

43 The development of analytical models for fan noise prediction has a long tradition, which is
 44 detailed in many papers, e.g. by Posson et al. [4]. Therefore, the intent of the subsequent review is
 45 not to be exhaustive but rather to highlight references that help to specifically understand the models
 46 included in this benchmark. Note that the references are not introduced in chronological order. Instead,
 47 the focus is on the works of Amiet [5] and Hanson [6], which are typical of two different modelling
 48 approaches, valid for a single isolated airfoil and a cascade of airfoils, respectively.

The notations introduced in Figure 1 will be used throughout the paper.

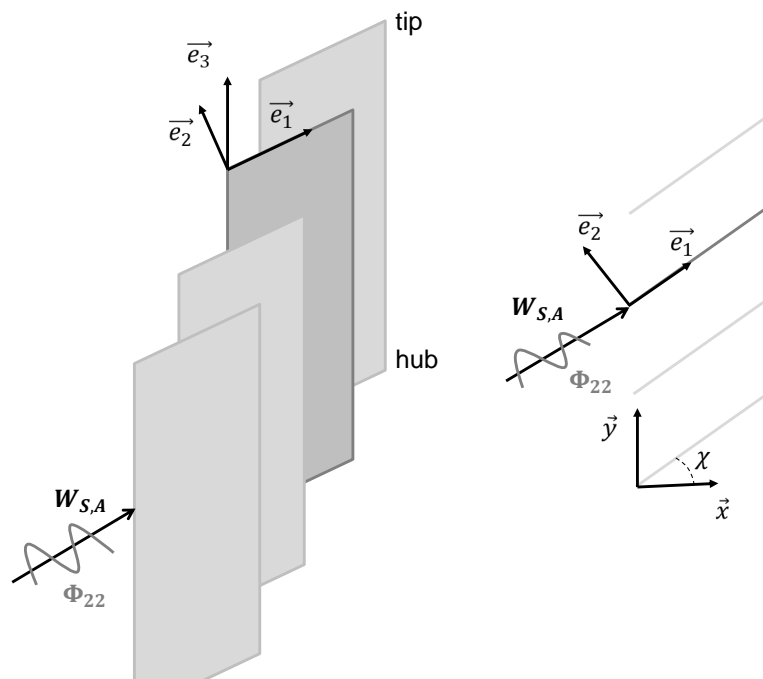


Figure 1. Notations as used in this paper for a rectilinear cascade of flat plates.

- 50 • (x, y, z) and (x, r, θ) refer respectively to a cartesian and a cylindrical coordinate system, where
- 51 the x -axis corresponds to the duct axis.
- 52 • $(1, 2, 3)$ are indexes referring to the streamwise, upwash and spanwise components of flow.
- 53 • The variable K refers to convective wavenumbers (of the incoming gust).
- 54 • The variable k refers to acoustic wavenumbers (of the radiated pressure waves).

55 In this context, an oblique gust is understood to be a vortical disturbances featuring a spanwise
 56 wavenumber component, i.e. $K_3 \neq 0$. On the contrary, K_3 is equal to zero for parallel gusts (the
 57 wavefront is parallel to the leading edge of the blades). Finally, regardless of the dimension of the
 58 turbulence wavenumber spectrum, the same notation Φ_{22} is used to denote the upwash velocity
 59 component. The dimension of the function is indicated by the number of dependent variables.

60 The first comprehensive theory to predict turbulence–airfoil interaction noise was formulated by
 61 Amiet [5] (1975). The author considered the case of homogeneous, isotropic turbulence impinging onto
 62 an isolated flat plate at zero mean-flow incidence. Amiet adhered to the acoustic analogy, specifically
 63 to the findings of Curle [7]. Consequently, he assumed that the unsteady lift produced by the upwash
 64 velocity component was the principal noise source mechanism. Amiet developed a formulation
 65 and an understanding of the problem, which is still the foundation for many of today’s models
 66 used to predict fan noise. If the turbulence is frozenly convected, Amiet showed that the turbulence
 67 representation required for the acoustic models can be simplified to a two-dimensional wavenumber
 68 spectrum obtained by integrating the three-dimensional wavenumber spectrum along its wavenumber
 69 component normal to the airfoil. For airfoils with a large aspect ratio, he further showed that the
 70 acoustic pressure in the plane at midspan can be calculated by only considering the component of the
 71 turbulence oriented parallel to the leading edge. The two-dimensional wavenumber spectrum retaining
 72 only parallel gust components is actually equal to the one-dimensional wavenumber spectrum
 73 multiplied by the spanwise correlation length of the upwash velocity component and by a factor
 74 $1/\pi$. As the one-dimensional wavenumber spectrum is easily measured by hot-wire anemometry, it is
 75 a useful turbulence representation to work with. To calculate the unsteady pressure jump, Amiet used
 76 a closed-form expression [8] based on the Sears function [9] for low frequencies and a successive
 77 approximation solution [10] for high frequencies. Amiet’s work demonstrated that a prediction of
 78 turbulence–airfoil interaction noise is achievable as long as the kinetic energy and integral length scale
 79 of the incoming turbulence are known.

80 An important milestone to consider more representative cases of turbomachines was marked by
 81 the work of Glegg in 1999 [11]. The author generalised previous analytical works on two-dimensional
 82 cascades of airfoils to derive a theory for three-dimensional rectilinear cascade of infinite-span swept
 83 blades interacting with three-dimensional harmonic gusts convected in a uniform cross-flow. Glegg
 84 solved the problem with the Wiener–Hopf technique. In that approach, the acoustic pressure is
 85 obtained directly without resorting to the acoustic analogy. To calculate sound power, an integration
 86 of the acoustic intensity [12] over the faces of the cascade was performed. For a given gust mode,
 87 Glegg identified an effective frequency, below which the generated pressure waves are evanescent.
 88 The cutoff–cuton transition is delayed when the spanwise component of the incoming gust or the
 89 blade sweep increase. Both effects are similar and are potentially beneficial for noise reduction. This
 90 was also shown in previous works by Graham [13] for an infinite, isolated plate. Graham proved that
 91 an oblique gust sweeping the airfoil’s leading edge at supersonic speed emits sound waves efficiently,
 92 while acoustic waves are evanescent if the trace speed is subsonic.

93 Based on Glegg’s cascade model, Hanson [6] (2001) developed a comprehensive theory to
 94 predict the broadband noise radiated by a cascade of blades with lean and sweep. As a first step,
 95 Hanson extended Glegg’s cascade theory to turbulent gusts. Hanson introduced several coordinate
 96 transformations to convert a cascade of blades as arranged in an annular duct into a cascade of
 97 rectilinear blades. Besides isotropic turbulence, he also considered the case of axisymmetric turbulence
 98 using the model proposed by Kerschen and Gliebe [14]. He further extended the method to integrate
 99 the case of inhomogeneous turbulence distribution featuring a higher level of turbulence in the rotor

100 wakes. Finally, he generalised the solution to rotating blades. Hanson proposed to apply a strip-based
101 approach, which consists in dividing the stator into radial slices, in order to take into account the
102 radial variation of the turbulence characteristics and of the geometry. The sound power is obtained
103 by summing up the contribution of all strips. Hanson performed comparisons of his calculations
104 (made for a typical radial position) to the experimental data of several fans covering a large range of
105 parameters. Because of a lack of experimental data, turbulence intensity and integrale length scales
106 were chosen to minimise the offset between predicted and experimental results. As an alternative to
107 this method of reverse engineering, Hanson identified the possibility of using RANS inputs for future
108 investigations.

109 Before Glegg's model was introduced, methods considering the cascade effect or blade-to-blade
110 interaction had relied on two-dimensional solutions in the plane ($\mathbf{e}_1, \mathbf{e}_2$). This option had been pursued
111 by Ventres et al. [15] (1982). In their approach, the acoustic analogy was applied using the fluctuating
112 load on the blades as source mechanism. As a benefit, the chosen approach enabled to consider
113 the duct acoustic effect by using the Green's function for an infinite annular duct expressed as an
114 infinite series of normal modes [12]. The strip theory approximation was applied. Thus, the rest
115 of the problem had been reduced to the calculation of the pressure jump on each strip as though it
116 were a linear cascade of two-dimensional, thin, flat plates. To obtain the blade pressure distribution,
117 Ventres and co-authors applied a numerical method solving an integral equation relating the source
118 strength of dipoles distributed on the plates to the velocity disturbance. The angle of the plates was
119 assumed to match the incoming mean flow angle. The turbulent velocity field was modelled by the
120 product of three Gaussian functions representing the spatial correlation of the turbulence in the three
121 directions. Thus, the strips were cross-correlated in the radial direction (\mathbf{e}_3) via the radial correlation of
122 the turbulence velocity, while the blade response remained two-dimensional.

123 In 2005, Nallasamy and Envia [16] first published a study dedicated to the prediction of fan
124 broadband noise based on a RANS-informed analytical approach. The Source Diagnostic Test (SDT)
125 fan rig equipped with three different designs of stator was used as a test case for the validation. The
126 comparisons were done at three operating points relevant for the acoustic certification: Approach,
127 Cutback and Sideline. The turbulence kinetic energy and the turbulence length scale at the stator
128 leading edge position were extracted from RANS $k - \epsilon$ simulations. The integral length scales were
129 defined based on standard hypotheses for homogeneous isotropic turbulence. The used acoustic model
130 corresponded to an extension of the Ventres' method, which cannot account for the effect of oblique
131 gust as mentioned before. Nallasamy and Envia were able to reproduce the general trends observed
132 experimentally although the slope at high frequency was overpredicted due to the use of Gaussian
133 functions to model the turbulence rather than the more physically realistic Liepmann or von Kármán
134 turbulence models.

135 Based on a similar approach to Nallasamy and Envia and still using the SDT case for validation,
136 Grace and co-authors published a series of papers, in which they investigated the sensitivity of the
137 analytical models regarding some of the assumptions. Thus, in 2012, Grace et al. [17] showed that the
138 method may create peaks with a high amplitude in the predicted noise spectra, which are not present
139 in the measurements. These peaks are linked to resonances of the two-dimensional cascade model,
140 that are much weaker for non-parallel blades. Grace et al. also started to investigate the validity of
141 their formulation, in which the three-dimensional wavenumber spectrum $\Phi_{22}(K_1, K_2, K_3)$ is replaced
142 by a two-dimensional wavenumber spectrum multiplied by a radial correlation function, denoted
143 by $\Phi_{22}(K_1, K_2)R_r(r)$. For one example, they found results that were significantly different between
144 the two approaches. The computation of the three-dimensional cascade response, required for the
145 exact approach, was a time-consuming process at high frequency, which explains the few frequencies
146 considered in the study. In the same paper, Grace et al. found that modeling the inhomogeneity of the
147 turbulence in terms of energy and length scale across the passage is not important (provided that an
148 appropriate turbulence averaging is applied as recently showed by Kissner et al. [18] by applying an
149 hybrid numerical method coupling the generation of synthetic turbulence and the linearised Euler

150 equations). An analysis of the correlation lengths by Grace et al. indicated that none of the known
151 isotropic models of turbulence could well reproduce the experimental data. They concluded that
152 anisotropy is important. Finally, they found no "correct" solution for determining the stagger angle
153 of the cascade. Whatever the chosen inclination was, no good agreement in amplitude and phase
154 between the analytically calculated pressure jump across the blade surface and an accurate numerical
155 solution accounting for the real blade geometry could be observed.

156 One year earlier, Grace et al. [19] published a sensitivity study of the RANS turbulence model, in
157 which they highlighted the fact that an accurate prediction of the turbulence intensity and turbulent
158 length scale of background turbulence can be of importance to obtain a good match with the
159 measurements. They found that the plate angle have a significant impact on the noise prediction¹.
160 In their results, by choosing the trailing edge rather than the leading edge as the plate angle, the
161 broadband noise spectrum at the exhaust is changed so that the levels are lowered at low frequency
162 but increased at high frequency. On the upstream side, the impact is more substantial as shown by
163 Jaron et al. [21], since a global decrease of the noise of several decibels can occur. An explanation
164 for that behaviour, which is linked to the orientation of the dipole sources with respect to the duct
165 cross-section, was proposed by Blandeau et al. [22]. Grace and co-authors were also interested in the
166 definition of the length scales for RANS simulations. They evidenced its importance for the acoustic
167 results.

168 In 2015, Grace [23] extended once again Ventres's solution to three-dimensional gusts. This time,
169 the unsteady response of the cascade to a three-dimensional vortical disturbance was solved by using
170 the integral equation approach of Ventres together with the similarity rules proposed by Graham [13].
171 Graham's similarity rules relate a three-dimensional gust to a two-dimensional problem. Grace showed
172 that only considering parallel gusts (i.e. only retaining the contributions for $K_3 = 0$) led to a strong
173 underestimation of the sound power levels by about 20 dB over the relevant frequency range. Setting
174 the unsteady vane response to the same value as that obtained for $K_3 = 0$ ($\forall K_3$) produced a good
175 agreement at high frequency but an overprediction at low frequency. A similar result was achieved by
176 using the two-dimensional solution.

177 Adopting an approach similar to Ventres, but using a three-dimensional solution [4] for the
178 unsteady blade loading derived from an extension of Glegg's model, Posson et al. [24] (2011) first
179 developed a method to account for three-dimensional gusts in annular ducts. The unsteady loading
180 was used as a distribution of dipole sources in the acoustic analogy together with the strip theory
181 approach. To avoid having some of the drawbacks linked to the rectilinear cascade hypothesis, Posson
182 et al. [25] proposed some corrections, in particular to minimise the resonance effects related to the
183 presence of parallel, adjacent blades. As the hub-to-tip ratio decreases, the formulation is increasingly
184 less exact and the solution is more prone to resonances. Finally, it should be noted that comparisons
185 between Posson's model and some of the other models cited above (Ventres, Hanson, Amiet) using the
186 SDT experimental results for validation were presented e.g. by de Laborderie [26] and Lewis et al. [27].
187 Their results evidenced discrepancies between the models, especially at low frequency. Accounting for
188 the cascade effect for skewed gusts greatly improved the prediction compared to solutions calculated
189 either with a two-dimensional cascade model or with an isolated-airfoil model. The presence of the
190 duct proved to be important too.

191 As shown by the literature review, the validation of RANS-informed analytical methods has been
192 mostly restricted to the SDT data provided by NASA. The present study uses a new, independent
193 data set obtained in 2018 at AneCom AeroTest during a test campaign organised in the framework
194 of the European project TurboNoiseBB [28]. These data give the opportunity to further assess the
195 RANS-informed analytical method. With the two questions raised at the beginning of the introduction

¹ For a stator, the difference of angle between the leading edge and the trailing edge depends on the fan loading as explained e.g by Moreau and Guérin [20]. For the SDT as for the ACAT1 fan, this difference is about 30 to 40°.

in mind, a benchmark was organised reconsidering the impact of the two main ingredients of the method: 1) the RANS calculation (in particular the choice of the turbulence model) and 2) the aeroacoustic models. While the first part of the study is addressed in a companion paper by Kissner et al. [1], this second part deals with the impact of the acoustic models. The benchmark character is unique as more than ten independent European institutions using different CFD and acoustic solvers were involved. This large diversity guarantees that several key aspects of the RANS-informed analytical approach for fan broadband noise were addressed.

The paper is structured as follows. The methodology to prepare the benchmark is described and the common input data for the noise calculation are presented. Then the acoustic prediction models are briefly introduced. Finally, the results are analysed in terms of the prediction of absolute levels and trends.

2. Benchmark Preparation

Section 2 provides some relevant information regarding the benchmark, including an overview of the data delivered to the participants.

2.1. ACAT1 Fan Benchmark Data

2.1.1. Tests at AneCom AeroTest

A short description of the TurboNoiseBB test campaign, which provided the validation data for the benchmark, was given by Guérin et al. [29]. Specific details on the instrumentation and data post-processing can be found in several publications [30,31]. The ACAT1 fan is a transonic fan composed of 20 rotor blades and 44 stator vanes. A longitudinal cut of the AneCom test rig is shown in Fig. 2. The noise instrumentation is highlighted in red. Two configurations with different rotor–stator gaps were measured in the project TurboNoiseBB but only the short gap variant was considered for the benchmark. Furthermore, the focus was restricted to the three operating conditions relevant for acoustic certification: Approach, Cutback and Sideline. These points were distributed along a single, the so-called “Sea Level Static” working line. Note that the stator geometry was simple, with no lean and nearly no sweep. According to Hanson [6], sweep has no significant effect for low angles as the peak amplitude is approximately proportional to the cosine of the sweep angle, hence $\Delta PWL_{peak} = 10 \log_{10}(\cos \phi_{sweep})$.

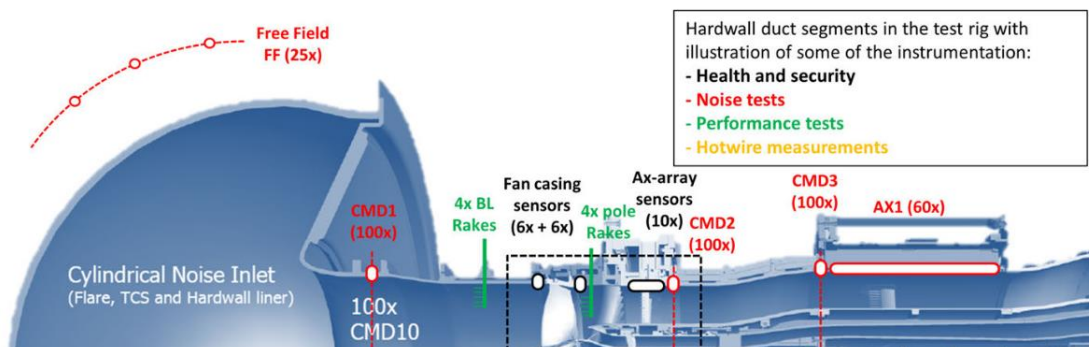


Figure 2. UFFA rig of AneCom AeroTest with the instrumentation used during the tests (TurboNoise consortium, reprint with permission).

2.1.2. Acoustic Data

The acoustic and aerodynamic tests were conducted separately in order to avoid a contamination of the acoustic results by the instrumentation (hot-wire probes and total pressure sensor rakes mounted along the stator leading edge). The noise results for the bypass duct are based on measurement data provided by the line array of condenser microphones AX1 indicated in Fig. 2. The microphones were

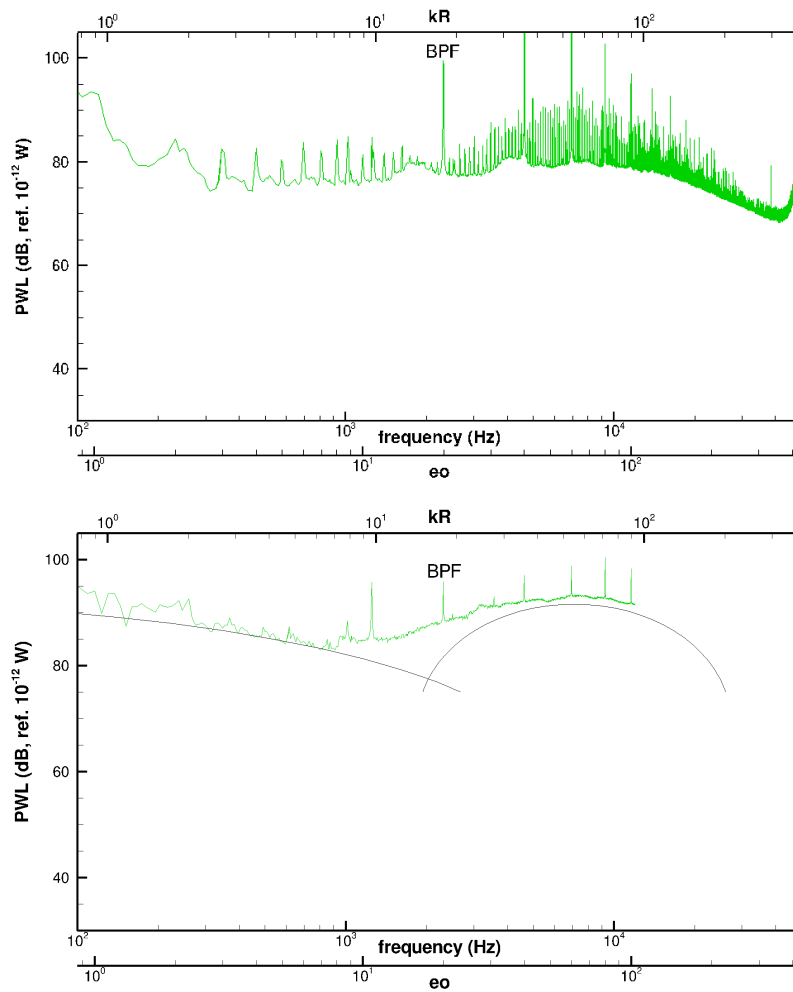


Figure 3. Sound power spectra at Sideline used for the comparison with the predictions: **(top)** far-field result in the forward arc including the tones, **(bottom)** result found in the bypass duct after removing the rotor-locked components.

229 wall-flush mounted in a section of constant radii located far downstream of the stator. The microphone
 230 signals were filtered using an axial wavenumber decomposition technique to efficiently separate
 231 hydrodynamic and acoustic pressure fluctuations [32]. The signals were synchronised with the rotor
 232 shaft so that the rotor-locked part of the fluctuations could be removed [33]. The model used to deduce
 233 the sound power spectra based on the sound pressure assumes an equal energy density distribution
 234 between the propagating acoustic modes of the same frequency band [32,34]. Very similar results were
 235 obtained by Pereira and Jacob [35].

236 The results in the forward arc are less prone to uncertainty as they were obtained by integrating
 237 the sound pressure spectra measured by the far-field microphones weighted by the sinus of the
 238 radiation angle. As the mean velocity in the plenum is very small it could be neglected. Contrary to
 239 the in-duct results, the far-field measurements were not rotor-synchronised. Therefore, the tones are
 240 strongly present in the spectra.

241 The results for the Sideline conditions are shown in Fig. 3. Two curves were drawn per hand on
 242 the downstream results to suggest the presence of at least two major sources of broadband noise which
 243 are present in the results. The peak frequency in rotor-stator interaction broadband noise is around
 244 $3 \times \text{BPF}$ but the low frequency levels seem to be dominated by another source.

| Short Gap: | Approach (AP) | Cutback (CB) | Sideline (SL) |
|-----------------------|---------------|--------------|---------------|
| rpm | 3856.1 (50%) | 6175.1 (80%) | 6945.7 (90%) |
| massflow (kg/s) | 54.85 | 88.80 | 101.32 |
| corr. rpm | 3797.9 | 6077.3 | 6836.5 |
| corr. massflow (kg/s) | 56.48 | 91.61 | 104.53 |

Table 1. True and corrected operating conditions on SLS working line measured during the acoustic tests.

2.2. Input for the Analytical Models

2.2.1. RANS Calculations

As the flow Mach number is one of the key parameter for fan noise, it was decided to extend the benchmark, which was focused on the condition Approach in Part I, to two more operating conditions, namely Cutback and Sideline. The corresponding values of rotation speed and mass flow are provided in Tab. 1. The structure of the flow differed significantly between the three operating conditions (see Guérin et al. [29]). At Approach, the flow detached at the leading edge as the rotor was highly loaded. This flow separation observed in the RANS calculations could not be evidenced as such by the experimental data. Due to a reduced rotor loading, no flow detachment was found at the highest investigated speed.

As shown in Part I of the benchmark, the choice of the turbulence model has a substantial impact on the predicted acoustic levels. All the RANS solutions used in Part II were produced by DLR with the CFD solver TRACE [36] using the Shear-Stress-Tensor (SST) $k - \omega$ turbulence model from Menter [37]. For Approach, this corresponds to solution RANS #2 presented in the Part I paper[1]. This turbulence model seems to be predominately used in the community. In fact, the study of Part I has shown that the agreement between CFD and the hot wire measurements is not satisfactory for any of the studied turbulence models. The hot-wire measurements data could not be used either, because of the current uncertainty in the data, in particular at high speed. As a consequence, the goal of the present benchmark was not to find out the most suitable acoustic model, but to investigate the relative impact of the model assumptions on the acoustic predictions and to quantify the variations.

2.2.2. RANS Data Processing

For a given operating point, all the acoustic simulations were based on the same input obtained by analysing the geometry and the flow solution of the RANS calculation. The data analysis – done with the DLR in-house tool *C3D_T2P* – was conducted at 97 radial positions equally distributed along the whole span (see Fig. 4). The streamline positions in the (x, r) -plane were determined after having circumferentially averaged the mean flow. Only the part of the flow going into the bypass duct was considered in the prediction. Thus, the interaction with the Engine Support Stator (ESS) located at the core entry was ignored. For each radial position of the stator, the following values were provided: the axial and tangential speeds up- and downstream of the stator (see Fig. 5), the turbulent kinetic energy and the turbulence length scale (see Fig. 6). Additionally, averaged values of the speed of sound and of the mean flow density calculated upstream of the leading edge were provided. Only one acoustic code was able to consider the real airfoil geometry. In the other models, the stator vanes are replaced by flat plates, whose stagger angle varies along the span (see Fig. 7).

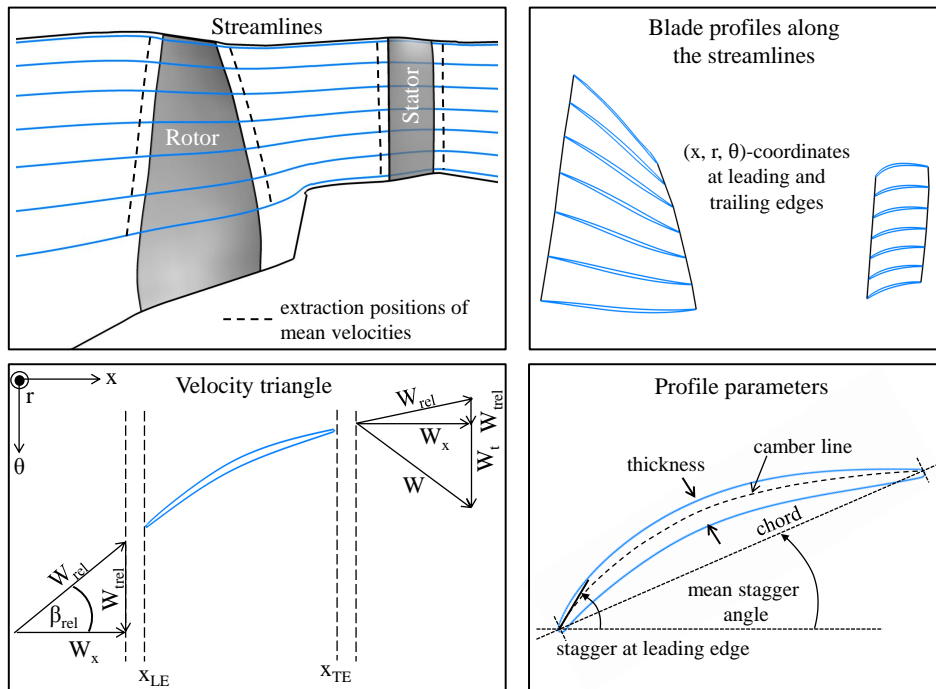


Figure 4. Extraction of geometry and flow parameters with the post-processing tool called *C3D_T2P* (Guérin et al. [29] adapted from Jaron [39], reprinted with permission).

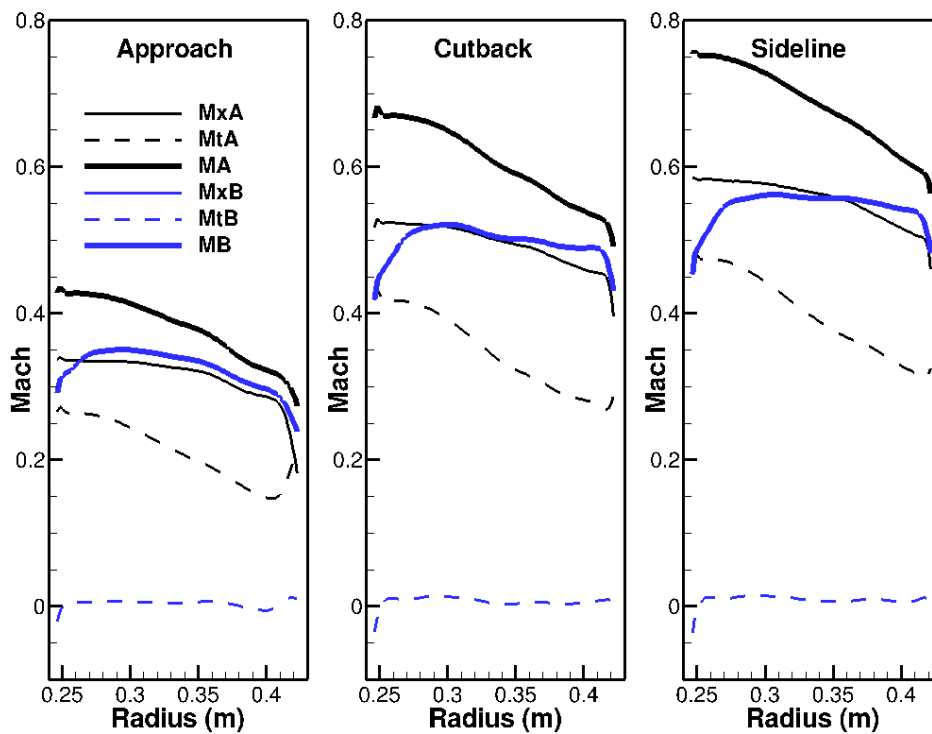


Figure 5. Spanwise distribution of the axial, tangential and total Mach numbers obtained by circumferential averaging at (A) a quarter chord length upstream of the leading edge and (B) a quarter chord length downstream of the stator.

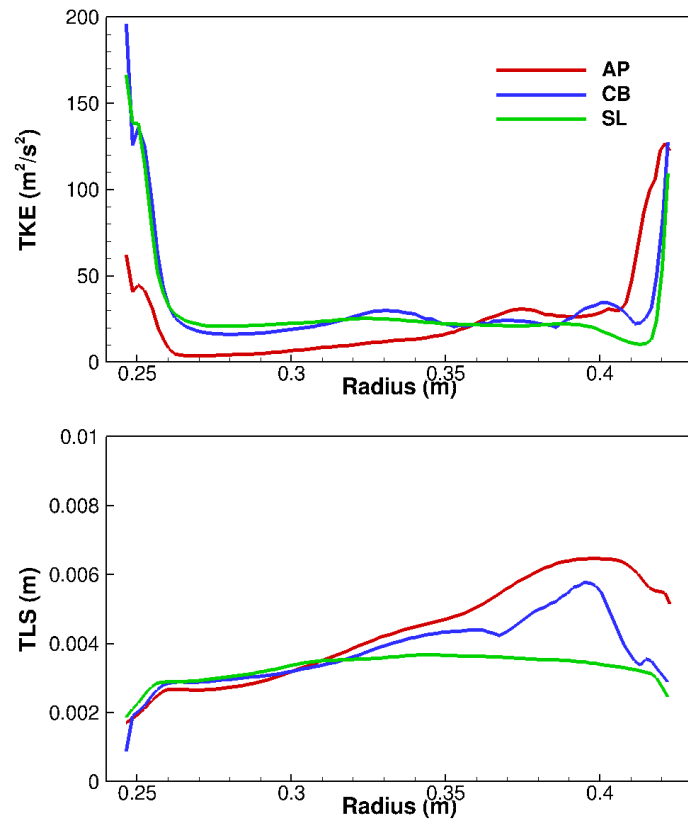


Figure 6. Turbulent kinetic energy \bar{k}_{RANS} (**top**) and turbulence length scale $\bar{\Lambda}_{RANS}$ (**bottom**) reconstructed at the stator leading edge for the three investigated operating points.

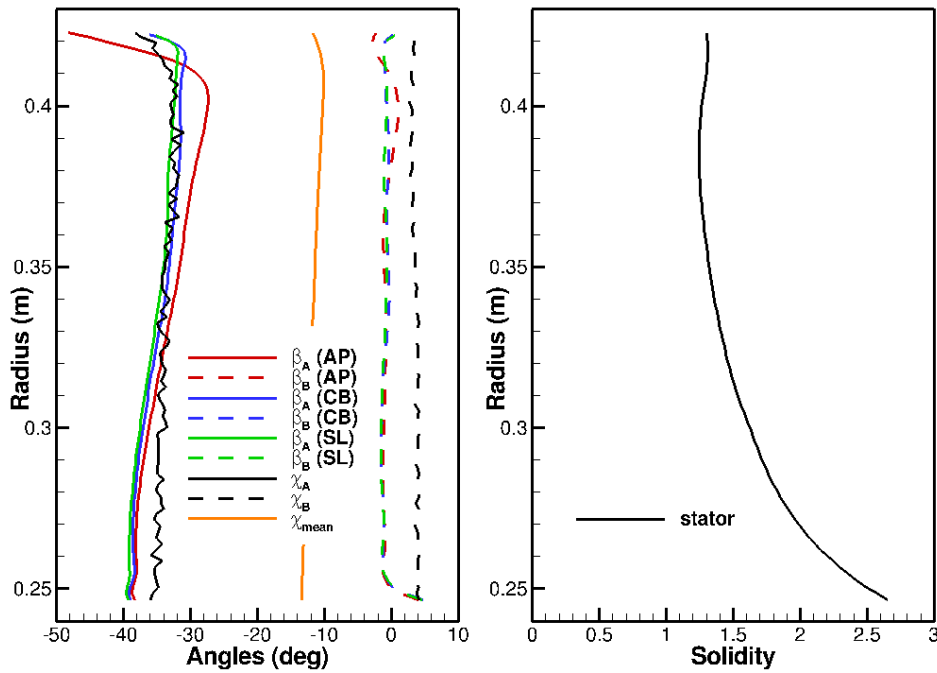


Figure 7. Spanwise distribution of (**left**) the flow (β) and stator (χ) angles, and of (**right**) the stator solidity (chord-to-pitch ratio).

278 Background and wake turbulence contributions were averaged and modelled by one single
 279 contribution having equivalent TKE and TLS values.

The turbulence kinetic energy \bar{k}_{RANS} was circumferentially area-averaged and the turbulence length scale $\bar{\Lambda}_{\text{RANS}}$ was weighted by the local value of TKE as proposed by Jaron et al. [21]:

$$\bar{k}_{\text{RANS}}(r) = \frac{1}{\Delta\theta} \int_0^{\Delta\theta} k_{\text{RANS}}(r, \theta) d\theta, \quad (1)$$

$$\bar{\Lambda}_{\text{RANS}}(r) = \frac{1}{\Delta\theta \bar{k}_{\text{RANS}}(r)} \int_0^{\Delta\theta} k_{\text{RANS}}(r, \theta) \Lambda_{\text{RANS}}(r, \theta) d\theta. \quad (2)$$

From RANS, only a single integral length scale can be calculated locally. It corresponds to the average size of the largest energy containing eddy. The local value of the turbulence length scale Λ_{RANS} was calculated based on the local values of k and ω^* , where ω^* is the specific turbulence dissipation rate [38]. The following relationship was applied:

$$\Lambda_{\text{RANS}}(r, \theta) = C_\Lambda \frac{\sqrt{k_{\text{RANS}}(r, \theta)}}{C_\mu \cdot \omega_{\text{RANS}}^*(r, \theta)}, \quad (3)$$

280 with the two constants $C_\mu = 0.09$ and $C_\Lambda \approx 0.4$. As a consequence of this averaging technique,
281 background and wake turbulence are mixed. Further ways to determine the turbulence integral length
282 scale are discussed in the companion paper [1].

283 Note that the turbulence characteristics were extrapolated downstream of the mixing plane up to
284 the stator leading edge position by using the reconstruction method based on a semi-empirical model
285 proposed by Jaron [39]. This extrapolation aimed at improving the comparison to the experimental
286 data. Indeed as the turbulence in the rotor wakes is convected towards the stator, its intensity tends to
287 decrease, while its length scale tends to increase. These two effects shift the peak frequency to a lower
288 value and produce a slight increase of the peak amplitude as shown in Part I.

289 3. Acoustic Models

290 Some general features of the acoustic models of the benchmark are presented in preamble to a
291 more detailed analysis of the models.

292 3.1. Preamble

- 293 • All methods of the benchmark are formulated in the frequency domain. They target a
294 representation of broadband noise in the form of a frequency spectrum but not as a time signal.
- 295 • It was assumed that broadband noise was generated by the interaction of the incoming turbulence
296 with the blades. Other sources of broadband noise like rotor self-noise, stator self-noise and
297 rotor-ESS interaction noise were ignored for the benchmark.
- 298 • The turbulence was assumed to be homogeneous, isotropic turbulence at each radial position/for
299 each strip. In all calculations, the turbulence was imposed as if it were a background turbulence
300 but of course using the equivalent TKE and TLS values of the benchmark, which include the wake
301 and background contributions.
- 302 • Either the von Kármán or the Liepmann model was used to describe the turbulence. The
303 difference between the two models is rather small. In fact, the differences are smaller than
304 1 dB for the one-dimensional wavenumber spectrum. As observed by Grace [23], the agreement
305 with experiments is better using the Liepmann model than using the Gaussian model.
- 306 • Most of the methods are mathematical expressions containing integrals and summations. A
307 few methods resort to a very complex modelling of RSI noise, which has a direct impact on
308 computation time. The latter can potentially exceed one day as reported by Grace [23]. The
309 solution labelled BB1 is partly numerical as it used a CAA solver to calculate the acoustic response
310 of the stator. That method was the only one able to account for the real blade profile including the
311 effects from the mean flow.

- 312 • All other methods replaced the stator vanes by flat plates as isolated airfoils or arranged in a
 313 cascade. The “flat plate” hypothesis implies that the most representative stagger angle is used.
 314 All the methods relied on the angle at the leading edge except for results TA1 and TA2, which
 315 considered the inflow angle. As the flow incidence is small at the stator leading edge, no strong
 316 effect is expected from that choice, even though the stagger angle is known to be a sensitive
 317 modelling parameter.

318 3.2. Classification of the Methods

319 The methods used for the benchmark were classified into two different categories. The result of
 320 that classification is shown in Fig. 8. One group contains methods that explicitly refer to the acoustic
 321 analogy, while the other group contains methods that rely on a direct calculation of the pressure
 322 cascade response:

- 323 • Methods based on the acoustic analogy were assembled in **Group A**. The models use a source
 324 term (the unsteady lift produced by the turbulence on the blade surface) in combination with a
 325 Green’s function to calculate the acoustic pressure. They either make the assumption of a single,
 326 isolated airfoil or consider a cascade of airfoils.
 327 • The methods of **Group B** follow a different approach. They rely on a direct calculation of the
 328 acoustic pressure response of the cascade of blades without requiring a source term. Therefore
 329 there is one step less in the workflow represented in Fig. 8. All of the studied methods account for
 330 the cascade by considering separate radial strips. These strips are then unwrapped to match the
 331 theoretical case.

332 Tables A1 and A2 in Appendix A summarise some important characteristics of the models and refer to
 333 the publications where more details can be found.

334 3.3. Methods Based on the Acoustic Analogy (Group A)

335 Approaches of Group A all rely on the acoustic analogy as mentioned before. To get an acoustic
 336 pressure, two main steps are necessary: 1) the calculation of the unsteady pressure distribution on the
 337 plates created by the vortical disturbance and 2) the integration along the stator radius of the source
 338 term multiplied by the appropriate Green’s function. The result is a distribution of the pressure at
 339 any point in space, which can then be used to calculate the sound power. Two options are possible
 340 regarding the calculation of the pressure jump on the surface of the plates. Five of the six methods
 341 considered that the blades are isolated but used different unsteady lift response models. The sixth
 342 method considered the cascade effect, i.e. accounted for the blade-to-blade interactions. Regarding
 343 turbulence, three solutions assumed that the gusts impinged parallel to the leading edge, while the
 344 other three methods accounted for the oblique component. Concerning the choice of the Green’s
 345 function, two options were tested in the benchmark. Two solutions considered the Green’s function in
 346 free-field with a uniform axial mean flow as if there were no hub and no casing surrounding the stator.
 347 Four solutions resorted to the Green’s function for an infinitely long annular duct with a uniform axial
 348 mean flow. This last Green’s function is expanded in normal modes [2,12].

349 The methods of Group A are now described, starting with the one implemented in the solver
 350 PropNoise. The latter is presented in more detail than the other methods as it was used to perform all
 351 the noise calculations presented in Part I of the benchmark [1]. Even though all methods in Group A
 352 are different, they must follow the same key steps.

353 3.3.1. Solutions PN1 and PN2:

354 The methods implemented in the DLR in-house code PropNoise [40] is among the simpler
 355 methods used in the benchmark. It is subsequently presented using the formalism of Moreau and
 356 Guérin [41]. The objective is to enumerate the various steps necessary in order to obtain a noise
 357 prediction based on RANS data and to illustrate the ambiguity and complexity of some choices.

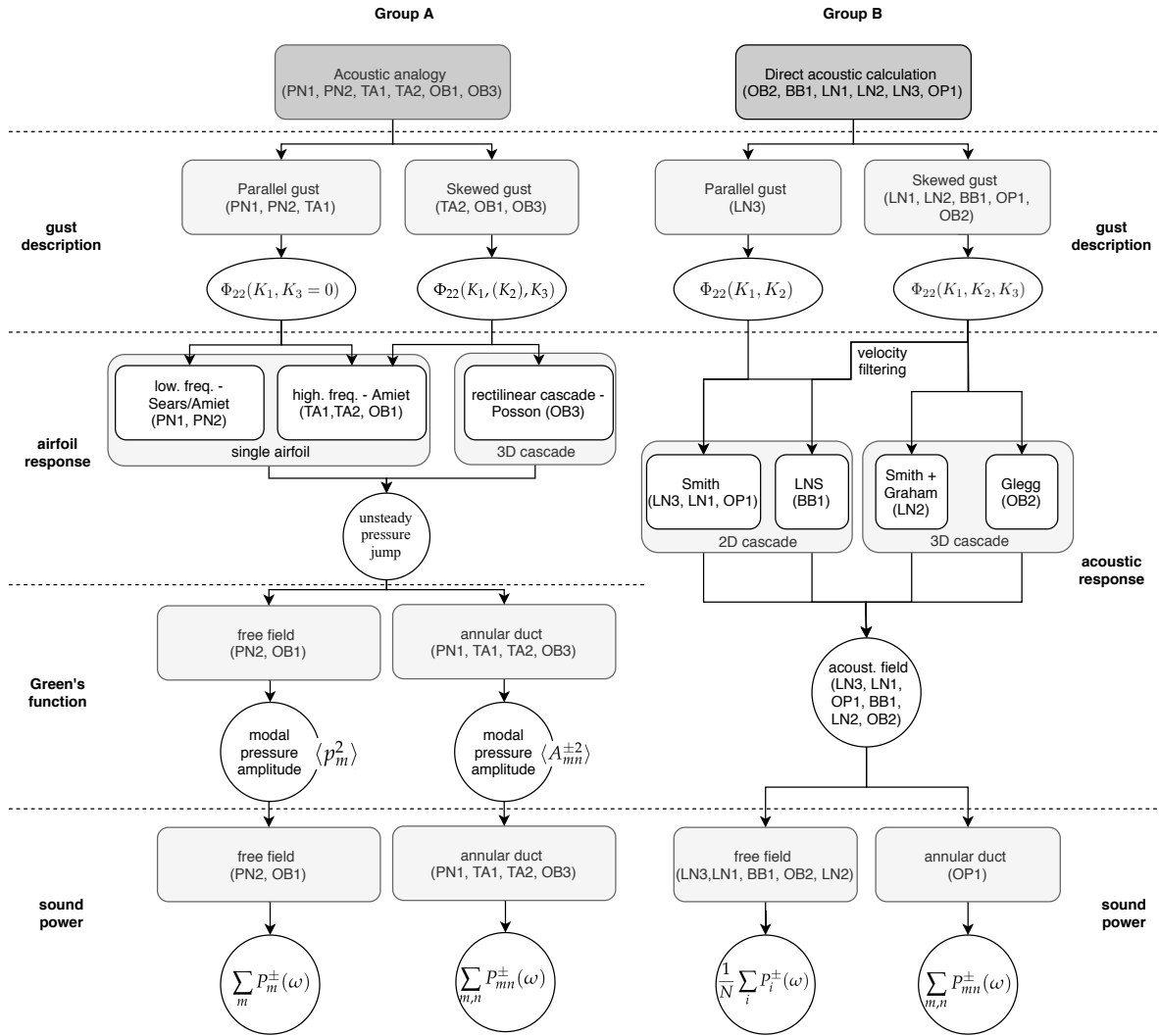


Figure 8. Classification of the models used in Part II of the TurboNoiseBB benchmark.

358 As mentioned before, the acoustic prediction relies on the acoustic analogy. For the prediction
 359 of RSI noise, only the source term related to the vane unsteady loading mechanism is considered.
 360 The other contributions e.g. due to the turbulence–potential-field interaction are not modelled. The
 361 unsteady loading is calculated by assuming that the vanes are isolated, which means that blade-to-blade
 362 interactions are not considered.

For a harmonic gust, Moreau and Guérin [41] showed that the pressure complex amplitude A_{mn} of the in-duct acoustic mode with azimuthal and radial orders m and n , at angular frequency $\omega = 2\pi f$, can be written as

$$A_{mn}^{\pm}(\omega) = iV \int_{\eta R}^R \hat{g}_{mn}(\omega, r) \exp(-ik_x x_{LE}(r) - im\theta_{LE}(r)) \sigma_{mn}(\omega, r) dr, \quad (4)$$

363 with the superscript \pm indicating the direction of propagation of the waves (“–” for upstream and
 364 “+” for downstream), V the number of vanes, R the tip radius at the vane, η the hub-to-tip ratio, r the
 365 radial position, x_{LE} and θ_{LE} , respectively the axial and circumferential positions of the leading edge, \hat{g}
 366 the radial shape function, σ the source term and k_x the axial, acoustic wavenumber.

Broadband noise is represented by the expectation values $\langle \cdot \rangle$ of the pressure modes:

$$\langle A_{mn}^{\pm 2}(\omega) \rangle = V \int_{\eta R}^R |\hat{g}_{mn}(\omega, r)|^2 \langle \sigma_{mn}^2(\omega, r) \rangle l_r(\omega, r) dr, \quad (5)$$

367 where it was assumed that the radial correlation length of the source term l_r is small compared to
 368 the radial variations of \hat{g} and σ . Later, the correlation of the source term will be equated to the radial
 369 correlation length of the upwash component of the turbulence. For the derivation of Eq. (5), it was
 370 also assumed that turbulence is frozenly convected and that the vanes are uncorrelated. The derived
 371 equation is similar to what Ventres et al. [15] or Nallasamy and Envia [16] proposed as solution to
 372 describe the background turbulence contribution. Differences are essentially due to the fact that the
 373 cascade effect is ignored in PropNoise, which greatly simplifies the solution.

The source term σ in Eq. (5) is given by:

$$\langle \sigma_{mn}^2(\omega, r) \rangle = |k_{\perp, mn}(r)c(r)|^2 \cdot \left(\frac{1}{2} \rho_0 W_{S,A}^2(r) \right)^2 \langle C_L^2(\omega, r) \rangle \cdot |\Psi_{mn}(\omega, r)|^2, \quad (6)$$

374 where k_{\perp} is the component of the acoustic wavenumber normal to the vane in the $(x, r\theta)$ -plane, ρ_0 is
 375 the mean flow density, c is the vane chord, $W_{S,A}$ is the incident velocity at the stator leading edge, C_L
 376 is the unsteady lift coefficient, and Ψ is a chordwise correlation function.

377 The indices (m, n) are dropped in the following as well as the dependency upon r to simplify the
 378 writing style.

The vane is replaced by a flat plate whose stagger angle is assumed to be equal to the metal angle at the leading edge $(\chi_{S,A})$. The wavenumbers k_{\perp} and k_l , respectively normal and parallel to the blade chord, are calculated by projecting the axial (k_x) and azimuthal ($k_{\theta} = m/r$) components of the wavenumbers of each acoustic mode into a system of coordinates relative to the flat plate [41]. This yields the following relationships between the wavenumbers:

$$k_{\perp} = -k_x \sin(\chi_{S,A}) - k_{\theta} \cos(\chi_{S,A}), \quad (7)$$

$$k_l = k_x \cos(\chi_{S,A}) - k_{\theta} \sin(\chi_{S,A}). \quad (8)$$

For a harmonic gust, the unsteady lift coefficient C_L is calculated as follows:

$$C_L(\omega) = 2\pi \frac{u_{\perp}(\omega)}{W_{S,A}} S(\omega), \quad (9)$$

where u_{\perp} is the normal component of the gust relative to the vane and $S(\omega)$ is the incompressible Sears function [9]. Using the Sears' solution means that the velocity disturbances are assumed to be vertical to the vane surface and to travel parallel to the leading edge. The following solution is obtained for turbulent gusts:

$$\langle C_L^2(\omega) \rangle = 4\pi^2 \frac{\Phi_{22}(\omega)}{W_{S,A}^2} S^2(\omega). \quad (10)$$

Hereby, it was assumed that the transverse component of the wake turbulence corresponds to the normal component to the flat plate. The spectrum Φ_{22} corresponds to the one-dimensional wavenumber spectrum. The Sears function [9] in its low-frequency approximation form [12] is equal to

$$S(\omega) \simeq \frac{1}{\sqrt{1 + 2\pi\kappa}}, \quad (11)$$

379 where $\kappa = (\omega/W_{S,A})(c/2)$ is a reduced frequency.

The chordwise correlation function (a concept introduced by Hanson [42]) enables to account for the fact that the source is not acoustically compact [8]. This term is defined by

$$\Psi_L(\omega) = \frac{1}{c} \int_{l=0}^c h_L(l) e^{-ik_l l} dl, \quad (12)$$

where h_L is the non-dimensional chordwise distribution of the loading ($1/c \int_{l=0}^c h_L(l) dl = 1$). Admittedly, the distribution of the unsteady load is strictly valid for a compact gust but the use of an acoustic, non-compact term leads to correct trends at high frequency as shown by Jaron et al. [21]. The distribution of chordwise lift is assumed to be real, constant and independent of frequency as proposed by Sears:

$$h_L(l) = \frac{2}{\pi} \sqrt{\frac{c-l}{l}}. \quad (13)$$

Thus we obtain the following analytical expression for Ψ_L ,

$$\Psi_L(\omega) = \left[J_0 \left(k_l \frac{c}{2} \right) - i J_1 \left(k_l \frac{c}{2} \right) \right] e^{ik_l \frac{c}{2}}, \quad (14)$$

380 where J_ν is the Bessel function of first kind and order ν . The blade response model implemented in
 381 PropNoise is limited by two factors: 1) it inherently contains the hypothesis that only parallel gusts are
 382 relevant for broadband noise following Amiet's findings at midspan for an infinite long isolated airfoil
 383 in free field and 2) it uses the Sear's function as the blade response function, which is only correct at
 384 very low frequency.

The modal Green function \hat{g}_{mn} is given by

$$\hat{g}_{mn}(\omega, r) = \frac{i}{4\pi R} \frac{f_{mn}(r)}{k R \alpha_{mn}}, \quad (15)$$

385 where f_{mn} is the normalised radial eigenfunction, α_{mn} a cuton factor, and $k = \omega/c_0$. All these quantities
 386 as well as the derivation of acoustic power are defined in Appendix B. Note that an equivalent solid
 387 body swirl of rotational angular speed Ω_s is also considered. Its value is defined so that the swirl Mach
 388 number at the tip is the same for the velocity distribution of a free-vortex flow. The Green's function
 389 extension – valid for low swirl Mach numbers – has an impact on the cut-on frequency of the acoustic
 390 modes.

391 The turbulence is considered to be homogeneous and isotropic for each strip. Of course, this
 392 contradicts the radial variation of TKE and TLS observed in the simulations. However, since the radial
 393 correlation length is small compared to the distance over which significant variations of TKE and
 394 TLS happen, the assumption is presumed to be acceptable. The turbulence is convected by the main
 395 flow. The vector of velocity perturbations can be split into three components, $\mathbf{u}' = (u'_1, u'_2, u'_3)$. As
 396 illustrated in Fig. (1), index 1 denotes the streamwise direction, and indexes 2 and 3 define the other
 397 two directions. For simplicity, we define component 2 as the direction normal to the vane surface
 398 and component 3 as the radial or spanwise direction. Additionally, a three-dimensional wavenumber
 399 vector $\mathbf{K} = (K_1, K_2, K_3)$ is defined to represent the spatial evolution of the turbulence.

In PropNoise, only the upwash component u'_2 of the turbulence is considered in the calculation of the blade response function. The spectrum Φ_{22} used in Eq. (10) is obtained by integrating the three-dimensional wavenumber spectrum along the wavenumber components K_2 and K_3 :

$$\Phi_{22}(K_1) = \int_{-\infty}^{\infty} \int_{-\infty}^{\infty} \Phi_{22}(K_1, K_2, K_3) dK_2 dK_3. \quad (16)$$

As the turbulence is convected by the mean flow, the wavenumber K_1 satisfies the following relationship: $K_1 = \omega/W_{S,A}$. If Φ_{22} is a power spectral density, then it follows:

$$\Phi_{22}(\omega) = 2 \frac{\Phi_{22}(K_1)}{W_{S,A}}. \quad (17)$$

The factor 2 is attributed to the fact that unlike $\Phi_{22}(K_1)$, $\Phi_{22}(\omega)$ is a one-sided spectrum. The square of the rms value of the upswash velocity $\langle u_2^2 \rangle$ satisfies:

$$\langle u_2^2 \rangle = \int_0^\infty \Phi_{22}(\omega) d\omega. \quad (18)$$

400 The spectrum Φ_{22} is an interesting quantity as it is easily measurable e.g. by hot wire anemometry.

As shown by Amiet [5], the two-dimensional wavenumber spectrum for the parallel gust components, $\Phi_{22}(K_1, K_3 = 0)$, is related to the product of the one-dimensional wavenumber spectrum $\Phi_{22}(K_1)$ and the radial correlation length l_r :

$$\Phi_{22}(K_1, 0) = \frac{1}{\pi} \Phi_{22}(K_1) l_r(\omega). \quad (19)$$

401 This product appears in PropNoise, therefore its final formulation is equivalent to considering only
402 parallel gusts.

For each strip, a spectrum $\Phi_{22}(\omega)$ is calculated by means of the von Kármán isotropic turbulence model. Velocity amplitudes are obtained by assuming

$$\bar{k}_{\text{RANS}} = \frac{3}{2} \langle u^2 \rangle, \quad (20)$$

where $\langle u^2 \rangle = \langle u_1^2 \rangle = \langle u_2^2 \rangle = \langle u_3^2 \rangle$ for isotropic turbulence. The integral length scale Λ is set equal to the CFD value $\bar{\Lambda}_{\text{RANS}}$. The one-dimensional wavenumber spectrum for the von Kármán model [5] is given by

$$\Phi_{22}(\omega) = \langle u_2^2 \rangle \cdot 2 \frac{\Lambda}{2\pi W_{R,B}} \frac{1 + (8/3)z^2}{(1 + z^2)^{11/6}}, \quad (21)$$

where $z = St/St_0$ is a normalised frequency so that $St = \omega\Lambda/W_{R,B}$ and $St_0 = \sqrt{\pi}\Gamma(5/6)/\Gamma(1/3)$. The relative speed at the rotor exit $W_{R,B}$ is used to account for the fact that the wake turbulence is produced by the rotor. While passing from the rotor frame to the fixed stator frame, no Doppler effect is included. The radial correlation length $l_r(\omega)$ is determined using the following equation [5]:

$$l_r(\omega) = \Lambda \frac{8}{3} \left[\frac{\Gamma(1/3)}{\Gamma(5/6)} \right]^2 \frac{z^2}{\sqrt{1 + z^2}(3 + 8z^2)}. \quad (22)$$

The correlation length l_r reaches approximately the value Λ at its peak and tends to zero in the two directions $\omega \rightarrow 0$ and $\omega \rightarrow \infty$. The correlation length is one of the most sensitive parameters of the modelling as the noise amplitude is directly proportional to it and the peak frequency is inversely proportional to it. The integral length scale, the rms value of the velocity, the one-dimensional spectrum and the radial correlation length are all related by the following integral equation:

$$\frac{\Lambda}{2} = \frac{1}{\langle u_2^2 \rangle} \int_0^\infty \Phi_{22}(\omega) l_r(\omega) d\omega. \quad (23)$$

403 The results PN1 and PN2 differ in the applied Green's function used. The in-duct solution was applied
404 for PN1 and the free-field formulation for PN2. Once the pressure is known it is straightforward to
405 derive the sound power as the flow is assumed to be homentropic and irrotational.

- 406 • In-duct formulation (PN1): Based on $\langle A_{mn}^{\pm 2} \rangle$, a modal power amplitude P_{mn}^{\pm} is calculated for each
 407 cut-on mode (m, n) using the equations in Appendix B. For each frequency, the sound power is
 408 obtained by summing the modal contributions: $P^{\pm}(\omega) = \sum_{m,n} P_{mn}^{\pm}(\omega)$.
- 409 • Free-field formulation (PN2): The pressure amplitude $\langle p_m^2 \rangle$ for the azimuthal mode m is used to
 410 calculate the sound power P_m by integrating the sound intensity along the polar arc. The sound
 411 intensity is obtained by applying the Blokhintsev invariant technique [41,43]. The sound power
 412 integrated between the polar angle $\psi = 0$ and $\pi/2$ corresponds to the downstream radiation,
 413 and the part between $\pi/2$ and π to the upstream one. The sound power for each frequency is
 414 integrated by summation over m : $P^{\pm}(\omega) = \sum_m P_m^{\pm}(\omega)$.

415 3.3.2. Solutions TA1 and TA2:

416 The results TA1 and TA2 were calculated respectively by the codes TinA1D and TinA2D, which
 417 were both developed at ONERA. A detailed description of the implemented models can be found
 418 in e.g. Reboul et al. [44,45]. The results TA1 were obtained following a method that is in many
 419 respects similar to the one used for obtaining the solution PN1, including the use of the parallel
 420 gust assumption modelled by the product $\Phi_{22}(K_1)l_r(K_1)$. The principal difference between TA1
 421 and PN1 concerns the choice of the unsteady lift response function. While PropNoise relies on
 422 the low frequency approximation of Sears [9] enhanced by an acoustic, non-compact term, TinA1D
 423 uses the high-frequency approximation proposed by Amiet [46]. The latest method also enables the
 424 consideration of oblique components as required by TinA2D. For single harmonic gusts, the Amiet
 425 based solution is expected to be more accurate over a large part of the frequency range.

426 For the results TA2, the spanwise component of the gusts was considered. Indeed, the formulation
 427 implemented in TinA2D uses the two-dimensional wavenumber representation of the turbulence
 428 spectrum $\Phi_{22}(K_1, K_3)$. Amiet showed that under certain assumptions (simple flat plate of infinite span,
 429 spanwise constant mean flow and turbulence) the acoustic pressure across a vertical plane at midspan
 430 is the same for strictly parallel and oblique gusts. However, it is not clear how this equivalence can
 431 be transposed to RSI broadband noise as there are spanwise variations of the mean velocity, of the
 432 turbulence characteristics and of the airfoil geometry. Furthermore, the amplitude of the triggered
 433 in-duct acoustic modes strongly depends on the position and orientation of the dipole source. For
 434 example, the amplitude is null if the source is located at a node of the mode or if it is oriented such as
 435 the dipole axis is perpendicular to the phase angle of propagation of the mode [47].

436 3.3.3. Solution OB1:

437 The results OB1 were obtained using the method proposed by Amiet et al.[48], which is
 438 implemented in the code OPTIBRUI. That method resembles the one used for calculating the results
 439 TA2 but uses the free-field formulation of the Green's function instead of the solution for an annular
 440 duct. As an additional difference, a Liepmann spectrum was used to model the turbulence and the
 441 metal angle at the leading edge was chosen to equal the plate inclination rather than the flow angle.

442 3.3.4. Solution OB3:

443 The model developed by Posson et al. [24,25], implemented in OPTIBRUI, was used to produce
 444 the results labelled OB3. This model was presented in the introduction of the paper. It can account for
 445 complex effects, while still relying to the acoustic analogy approach. Contrary to the other solutions of
 446 Group A, Posson's model accounts for the cascade effect for three-dimensional gusts (based on a strip
 447 approach) using an extension of Glegg's solution [11]. This is the only model of the benchmark that
 448 combines a three-dimensional cascade approach and the Green's induct formulation.

449 3.4. Methods Based on a Direct Calculation of the Acoustics (Group B)

As mentioned above, the methods classified in Group B bypass the calculation of an acoustic source term; they determine a cascade response function R , which directly links the vortical disturbance

to a velocity potential fluctuation and eventually to an acoustic pressure. For a harmonic gust, which can be either two- or three-dimensional,

$$u_\mu(\mathbf{x}, \omega) = \hat{u}_\mu e^{i\mathbf{K}_\mu \cdot \mathbf{x}}, \quad (24)$$

the pressure field created by the interaction with the cascade can be written in short-hand notation as

$$p_\mu^\pm(\mathbf{x}, \omega) = \rho_0 U_0 \hat{u}_\mu \sum_{\nu=-\infty}^{\infty} R_\nu^\pm(\mathbf{K}_\mu) e^{i\mathbf{k} \cdot \mathbf{x}}, \quad (25)$$

450 where ν is a scattering index. This solution can be extended to turbulent gusts.

451 The cascade response is calculated using either the three-dimensional (3D) solution for a rectilinear
 452 cascade of blades derived by Glegg [11] or the two-dimensional (2D) solution, which can be calculated
 453 by several methods. The methods of Group B are facing specific problems. With Glegg's approach, a
 454 strip approach is needed for turbomachine applications because i) the geometry varies along the span
 455 (blades can be twisted), ii) non-parallelism is not considered, and iii) the mean flow and turbulence
 456 values vary radially. For two-dimensional approaches, the question arises of how passing to a
 457 three-dimensional solution and/or to a sound power amplitude. Several corrections, applied either
 458 before or after the calculation of the acoustic cascade response, were tried to counterbalance the fact
 459 that two-dimensional formulations do not account for oblique components.

460 3.4.1. Solution OB2:

461 The results labelled OB2 were obtained with OPTIBRUI by applying Hanson's method [6,49]
 462 as described in the introduction. Hanson's approach relies on Glegg's cascade response for
 463 three-dimensional gusts. Away from the blades, the acoustic waves propagate in a free field with an
 464 axial and a tangential mean flow corresponding to a flow field parallel to the flat plate modelling the
 465 blade. The acoustic intensity is calculated by integrating the velocity potential over the upstream (resp.
 466 downstream) faces of the cascade. Eventually, the problem is reduced to the calculation of a direct
 467 transfer function between turbulence and sound power spectrum for each strip. The final acoustic
 468 power is obtained by averaging the contribution of all strips.

469 3.4.2. Solution LN3:

The method applied for the results labelled LN3 was presented by Cheong et al. [50]. It relies on
 the two-dimensional cascade response model implemented by Whitehead [51] in the code LINSUB.
 That model is based on Smith's work [52]. An integral equation, which relates the source strength
 to the velocity disturbance, is solved by using a collocation procedure. The applied turbulence
 spectrum is the two-dimensional spectrum $\Phi_{22}(K_1, K_2)$ obtained by integrating the 3D wavenumber
 spectrum $\Phi_{22}(K_1, K_2, K_3)$ over its spanwise component K_3 . Through this integration, the contribution
 of subcritical waves such as

$$|K_3| < \frac{|K_1|M}{\sqrt{1-M^2}}, \quad (26)$$

470 are included even though they are acoustically cutoff.

471 Cheong and co-authors showed that there is a critical frequency below which the interaction
 472 between neighbouring blades is important to include. Above this frequency, the blades can be
 473 considered acoustically isolated.

474 3.4.3. Solution LN1:

475 The results labelled LN1 were also obtained with the solver LINSUB (see Blázquez and Corral [53]).
 476 Thus, the method to calculate the acoustic pressure relies on the same algorithm as for LN3. In order
 477 to minimise the just mentioned drawbacks of the 2D approach, the authors performed a filtering of
 478 the velocity spectrum prior to the acoustic calculation. The applied corrections are explained in the

479 subsequent paragraph describing the method used for BB1. Note that the simulations were good
 480 converged despite using only 5 strips. Indeed, instead of using the values at the mean radius of the
 481 strip, the authors performed some radial averaging beforehand.

482 3.4.4. Solution BB1:

483 The method applied to obtain the results BB1 was described by Blázquez and Corral [54]. It is
 484 similar in many respects to LN1. The main difference is the use of a linearized Navier-Stokes (LNS)
 485 solver called $Mu^2s^2T - L$ [55] to calculate the acoustic response instead of LINSUB. The objective of
 486 the BBNANEMS code is to work for turbomachine components like turbines, where e.g. the infinitely
 487 thin flat plate approximation is no longer satisfying. This way, the blade shape (camber and thickness)
 488 and its effect on the mean flow (overspeed at the leading edge and flow deviation between leading and
 489 trailing edge) can be considered. To save computation time, the calculations are done on a reduced
 490 number of 2D strips equally distributed in the radial direction. In principle, the method could be
 491 extended to 3D blade geometry but at the expense of a dramatic increase in computational cost. Notice
 492 that the LNS solver works with harmonic gusts and not with time-domain synthetised turbulence
 493 as done by e.g. Wohlbrandt et al. [56]. While the cascade response function R is calculated in two
 494 dimensions, the three-dimensional formulation of Eq. (25) is still retained, which means that the
 495 authors have to make some further assumptions:

- 496 • The cascade response is independent of the value K_3 and is set equal to the response obtained
 497 for $K_3 = 0$. Grace [23] showed that using that simplification leads to a good agreement at high
 498 frequency but an overestimation of the sound power at low frequency.
- 499 • To counteract that effect, convective modes that are acoustically cut-off (subcritical waves) are
 500 discarded to avoid having their contribution included.
- 501 • The resulting pressure is assumed constant over the radius.
- 502 • The sound power is calculated through the integration of the intensity over the cascade faces
 503 without accounting for the presence of the duct.

504 A sound power spectrum is calculated for each strip. The final power spectrum is obtained by
 505 averaging all the contributions.

506 3.4.5. Solution LN2:

507 The solution LN2 was obtained by extending the 2D method used for LN1 to the three-dimensional
 508 wavenumber spectrum by using Graham's similarity rules [13], a technique also applied by Grace [23].
 509 This allows to properly account for the contribution of the oblique gusts in the calculation of the
 510 cascade response function R . The sound power is calculated as for BB1.

511 3.4.6. Solution OP1:

512 The method to obtain the result OP1 is implemented in the code Orpheus of ITP. Its principle was
 513 described by Carrasco and Serrano [57]. The method is based on a 2D cascade response following
 514 Smith [52]. Contrary to the methods described previously, it aims to include the duct effect. If needed,
 515 the code Orpheus uses the technique of Nallasamy and Envia [16] to distinguish between background
 516 turbulence and wake turbulence.

517 For the present calculation, the turbulence was distributed uniformly along the azimuth as it were
 518 a background turbulence. The question of how to proceed in order to overcome the drawback of a 2D
 519 cascade response is addressed in 2 steps.

520 Three different options to represent the turbulence were proposed by the authors:

- 521 (1) The simplest approach uses a 2D (K_1, K_2) -wavenumber spectrum obtained by integrating
 522 Liepmann's 3D wavenumber spectrum over the spanwise component K_3 .

- 523 (2) An *a priori* correction is applied, which consists in filtering the 2D wavenumber spectrum by
524 discarding gusts, whose contributions are known to be acoustically cut-off. This automatically
525 lowers acoustic levels.
- 526 (3) The results of three-dimensional CAA calculations performed for few selected gust modes and
527 frequencies are combined to develop an *a priori* correction of the turbulence content.

528 To calculate the sound power, there were also three different options:

- 529 (a) The 2D acoustic power is calculated and then assumed to be constant over the span. The final
530 solution is obtained by statistically averaging the contributions of all strips.
- 531 (b) The pressure amplitudes are averaged and then distributed in acoustic duct modes (m, n)
532 according to a certain model (equal energy distribution, equal energy density distribution, etc.).
533 This emulates the approach used to determine sound power based on experimental data.
- 534 (c) An acoustic mean pressure is calculated by averaging the results of all the strips. The radial
535 pressure distribution is represented by a complex function, whose amplitude is constant to the
536 averaged value and the phase is randomly varied along the span. This radial pressure is fitted to
537 the basis of induct acoustic eigenmodes in order to determine the amplitudes A_{mn} . Finally, the
538 modal sound power P_{mn} is calculated following the method described in Appendix A.

539 The authors investigated different combinations of the presented options. They showed that option
540 (3,c) provides the closest results to experimental data, but several CAA computations need to be
541 performed in order to find the proper correction for the turbulence content. Results based on option (1)
542 are significantly overestimated, in particular at low frequency. Method (2) provides fair results but the
543 low- and high-frequency trends are better reproduced with method (3).

544 4. Results and Discussion

545 The results of Part II of the TurboNoiseBB benchmark using the solvers presented in the previous
546 sections are now presented. As the same RANS inputs were used for all simulations, the different
547 acoustic codes can be directly and fairly compared. However, it should be noted that differences
548 between simulations and experimental values should be interpreted very carefully as the acoustic
549 models are sensitive to the RANS input and the way the integral length scale is calculated, as showed in
550 Part I [1]. Furthermore, the experimental data are not limited to fan-OGV interaction broadband noise
551 but rather contain all aerodynamic noise sources of the test rig as briefly discussed in Section 2.1.2.

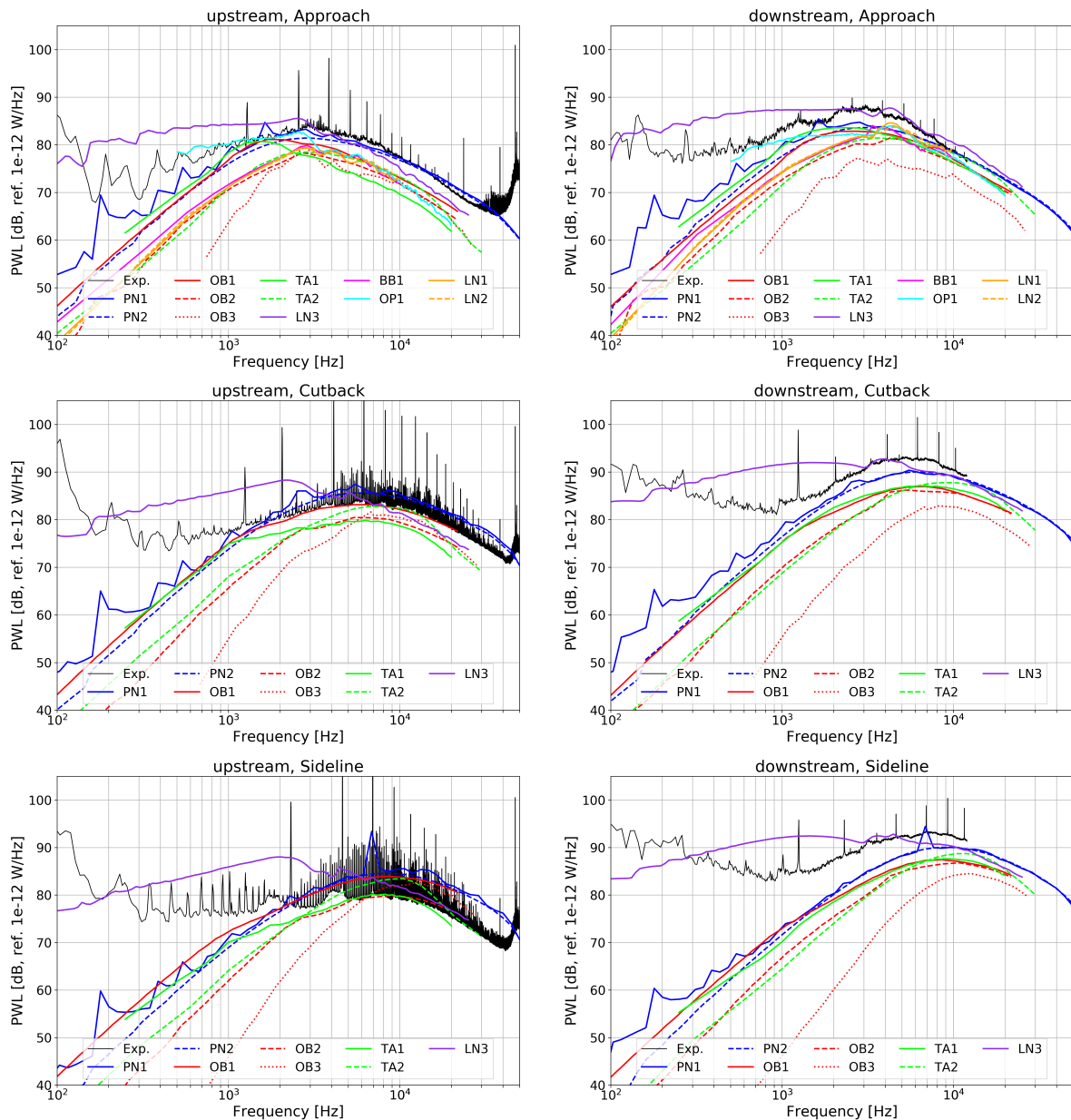


Figure 9. Acoustic results of the benchmark: **(left)** upstream PWL, **(right)** downstream PWL.

552 4.1. Overall Comparisons

553 At first, measured and predicted sound power spectra for the three operating points are compared
 554 (see Fig. 9). Note that some codes were only applied for the Approach operating condition. The
 555 following observations can be made:

- 556 • The prediction curves match satisfactorily with the experimental results at mid and high
 557 frequencies. All but one result deviate by less than ± 3 dB in that frequency range compared to a
 558 hypothetical median solution. The predicted peak frequency agrees with the experimental data,
 559 indicating that the RANS prediction of the integral length scale was acceptable.
- 560 • Greater differences are visible at low frequencies, yet most results remain within a similar range.
 561 The solutions LN3 and OB3 represent two extrema, respectively much higher and lower than the
 562 other ones.
- 563 • In general, the differences between two prediction curves remain the same for the up- and
 564 downstream positions.

- 565 • Compared to the experimental data, the predicted levels are underestimated downstream of the
 566 stator, except for LN3. At the upstream position, amplitudes are slightly overestimated in some of
 567 the results at high speed. This is possibly related to the fact that rotor shielding was not included
 568 in any of the simulations. At the higher speeds, the formation of shocks on the rotor blades blocks
 569 the transmission of RSI noise in the direction of the inlet (see the investigation by Blazquez and
 570 Corral [54] regarding the importance of blockage for the ACAT1 fan). This effect explains that the
 571 measurements at Sideline are lower than those at Cutback in the forward arc. A model accounting
 572 for rotor shielding would be necessary to improve the comparison with the far-field data in the
 573 forward arc.

574 4.2. Trends in Sound Power Split and by Speed Variation

575 Two further comparisons are done regarding i) the split of the sound power level between up-
 576 and downstream (see Fig. 10) and ii) the change in acoustic power by increasing the rotation speed (see
 577 Fig. 11). Experimental trends were not included in these analyses as a meaningful comparison cannot
 578 be realised because of the aforementioned rotor shielding and the presence of other noise sources
 579 included in the experimental data.

580 Regarding the power split between up- and downstream radiation, defined by $\Delta P_{dB} =$
 581 $10 \log_{10}(P^+ / P^-)$, three effects can have an impact on the results:

- 582 (1) Previous studies [6,19,21–23] showed the sensitivity of sound power to the choice of the stagger
 583 angle, in particular in the upstream direction. The flat plate assumption with the use of the
 584 leading edge stagger angle for inclination tends to overestimate the upstream contribution and
 585 underestimate the downstream contribution.
- 586 (2) The rotor shielding and to a lesser extent the swirl effect influence the balance in energy between
 587 the upstream and downstream radiations too.
- 588 (3) Finally, the mismatch between the unsteady loading formulation and the Green's function in
 589 methods of Group A is also a source of error.

590 As expected, the present benchmark indicates higher PWL values at the downstream side. The solution
 591 OB3 (Posson's model) is an interesting case as it deviates from the other predictions by its low difference
 592 between the upstream and downstream levels. Compared to the other predictions of Group A, this
 593 distinct behaviour may be attributed to the issue with the stagger angle, since effects (2) and (3) are
 594 common assumptions for all of the methods of Group A. Indeed, the stagger angle definition has
 595 three consequences: it impacts the streamwise component of the mean flow, the orientation of the
 596 dipole sources, and the cascade effect in the interblade channel. For isolated airfoils, only the first two
 597 effects are present, not the third one. Nevertheless, this differing behaviour is not observed for the OB2
 598 results (Hanson), even though the effect in the interblade channel is modelled too. Thus, it remains
 599 an unsolved issue. By separately analysing the solutions calculated with the single airfoil theory and
 600 those calculated with cascade models, one observes the following result: Using single airfoil models,
 601 the relative contribution of the downstream part increases with frequency. For some models, the
 602 difference ΔP_{dB} grows up to 10 dB at the upper frequency limit. With a decreasing frequency, the
 603 offset asymptotically approaches a value of zero. OB1 provides a good example for that trend. The
 604 solutions obtained using cascade models produce an interesting result: A minimum is present at a
 605 frequency around 2-3 kHz. This trend is most definitively visible at Sideline. On both side of the
 606 deep, the downstream contribution is superior to the upstream one. Unlike for single airfoil models, a
 607 tendency of ΔP_{dB} towards zero at low frequencies is not observed for the simulations performed with
 608 the cascade models. The results of Blandeau et al. [22] clearly indicate such a convergence - abrupt - but
 609 at very low frequency. For the ACAT1 fan, this convergence probably occurs at a frequency lower than
 610 the minimum frequency of 100 Hz considered in the benchmark, therefore it could not be documented.

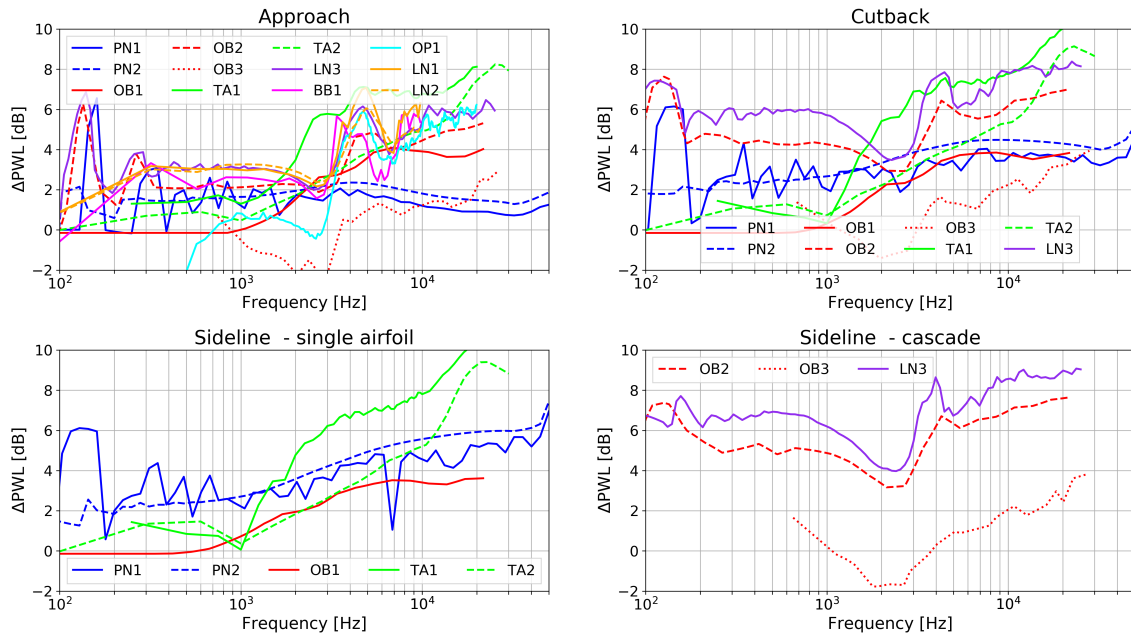


Figure 10. Sound power difference $\Delta P_{dB}(f) = PWL_{down}(f) - PWL_{up}(f)$; (a) Approach, (b) Cutback, (c,d) Sideline.

611 The trends due to the increase in rotational speed are much more harmonious as shown in Fig. 11.
 612 Those are principally driven by the change in the spectral shape of the prescribed velocity spectrum
 613 due to the changing turbulence characteristics. As all the partners used similar models to represent the
 614 spectral content of the turbulence, the agreement is reassuring but not surprising. Nevertheless, the
 615 fact that LN3 and OB3 follow contradictory trends and deviate significantly from all other solutions
 616 needs to be emphasised. Neglecting the rotor transmission effect, Hanson [6] observed that noise
 617 increases faster downstream – where the peak amplitude of sound power varies proportionally to M^5 –
 618 than upstream – where the peak amplitude varies proportionally to $M^{4.5}$. This tendency is also clear in
 619 the benchmark results, even though no effort was made to quantify the exponents.

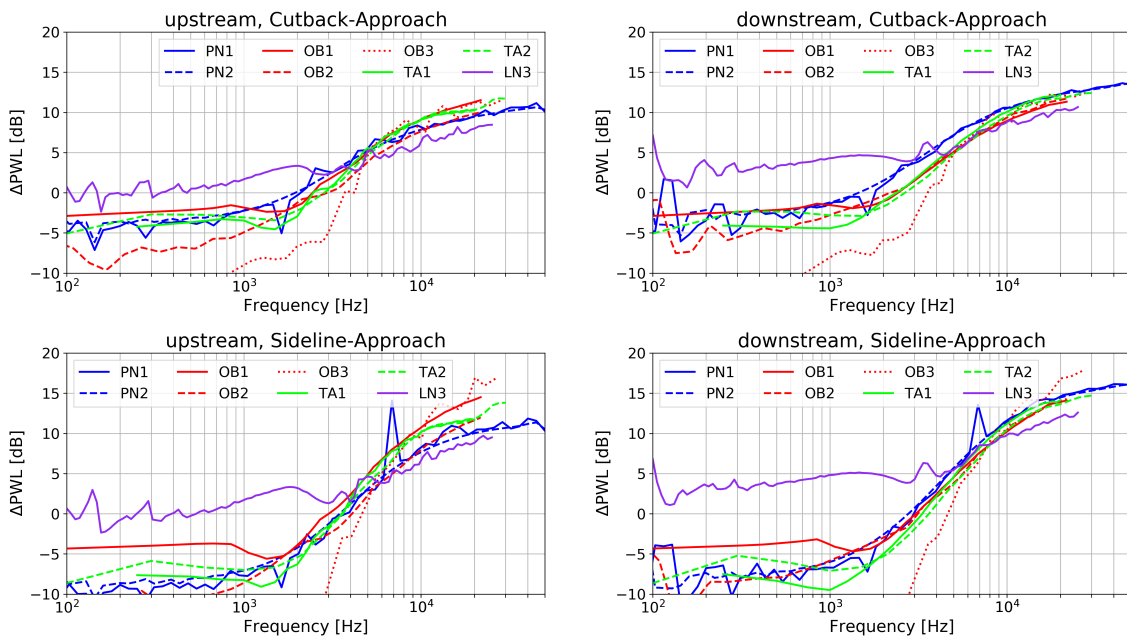


Figure 11. Acoustic change by increased speed: (left) upstream PWL, (right) downstream PWL.

620 4.3. Detailed Comparisons

621 The analysis below goes into more detail regarding some of the effects identified before as possibly
622 impacting predictions. It does not explicitly refer to the classification of the models into Group A and
623 Group B as the focus is on the differences in the models assumptions rather than on the differences in
624 the methods. Even though the two are closely related, they are not the same.

625 4.3.1. Effect of Acoustic Boundary Conditions

- 626 • The solutions PN1 and PN2 based on the in-duct and free-field formulations for the Green's
627 function converge asymptotically at high frequency (see Fig. 9, 10 and 11) as expected from e.g.
628 Moreau and Guérin [41]. The in-duct solution PN1 exhibits some peaks in the low-frequency
629 range, which occur when new in-duct acoustic modes become cut-on. These peaks are clearly
630 visible in the measurements, not only in the in-duct data downstream but also in the far-field data
631 upstream.
- 632 • Unfortunately, the comparison between TA1 and PN1 does not allow for a definite conclusion
633 regarding the importance of swirl as the two solutions also differ with respect to the Green's
634 function, the stagger angle, and the blade response. The agreement between TA1 and PN1 is
635 generally good (within 1-2 dB) at low frequency and fair (within 3 dB) at the downstream position
636 at high frequency. In the upstream direction, the mismatch is significant at high frequency
637 exceeding up to 8 dB. Supposedly, this behaviour is due to the different definition of the stagger
638 angle and the use of a different blade response function and is likely not related to the effect of
639 swirl.
- 640 • Compared to PN2, the swirl accounted for in PN1 has no significant effect on noise. Only a
641 slight noise increase at low frequency is observed with swirl. In fact, the acoustic modal content
642 is changed by considering the presence of swirl but the impact is small at medium and high
643 frequencies because of the statistically large number of cut-on modes. In fact, accounting for the
644 swirl may not be essential for RSI broadband noise prediction. This remark is not valid for sound
645 fields composed of only a few modes as for RSI tones. Indeed, it is important to include swirl in
646 order to properly determine the cut-on limits of acoustic modes, amongst other things.

647 4.3.2. Effect of Gusts Model

- 648 • The simulations TA1 and TA2 differ in the wavenumber representation of the gusts. In the
649 first simulation, all gusts are assumed to impinge on the stator with a wavefront parallel to
650 the leading edge ($K_3 = 0$). For the second case the spanwise component K_3 is included in the
651 simulations. The two models produce results, which differ significantly, in particular at low
652 frequency. Considering the oblique component leads to a decrease in sound power level by more
653 than 5 dB at low frequency and an increase by up to 3 dB in the mid range. The inversion point is
654 located slightly below the peak frequency. At high frequencies, the two solutions are more alike.
655 A similar trend was reported by Reboul [45] for a single airfoil in free field with a low aspect ratio.
656 Thus, the assumption that the contribution of oblique gusts is negligible as proposed by Amiet [5]
657 is not applicable to our case. Presumably, the levels are lower at low frequency in TA2, because
658 subcritical gusts are properly considered. Such an effect was also observed on cascade models
659 when accounting or removing subcritical gusts on the SDT case [23,24].
- 660 • A similar comparison can be done between the results LN1 (parallel gusts) and LN2 (oblique
661 gusts) for the cascade model. Contrary to the previous example, the results are close. This is due
662 to the fact that the subcritical gusts were removed *a priori* from the two-dimensional wavenumber
663 velocity spectrum $\Phi_{22}(K_1, K_2)$ used to calculate the solution LN1.
- 664 • The agreement between LN3 (two-dimensional representation of the turbulence spectrum) and
665 LN1 (two-dimensional representation of the turbulence spectrum with filtering of the subcritical
666 gusts) is good at high frequency but poor at low frequency, which supports the previous claims.
667 Note that the trends at low frequency presented by Cheong et al. [50] for a model test may

668 seem to be different from those shown here using the same code: unlike for the present ACAT1
 669 benchmark, the shape of the spectra corresponded to an inverse parabolic curve, typical of RSI
 670 broadband noise. Compared to the present study, the only differences in Cheong's paper were i)
 671 the representation in one-third octave bands, which changes the trend at low frequency compared
 672 to a representation in narrow bands, and ii) the fact that turbulence length-scale and intensity
 673 were adjusted to provide the best possible match to the measured data at high frequencies.

674 4.3.3. Impact of Airfoil-Response Model

- 675 • *In-duct Isolated Airfoil*: The results PN1 and TA1 can be analysed regarding the impact of the
 676 lift-response function. For that, the effect of swirl on the in-duct Green's function must be assumed
 677 neglected. The solution PN1 applies the low-frequency Sears' model enhanced by an acoustic,
 678 non-compact term [8], whereas TA1 relies on the Amiet's high-frequency approximation [46]. In
 679 the downstream section of the duct, there is a difference of approximately 3-4 dB between the two
 680 results. In the upstream section, the discrepancy is larger and increases with the Mach number. It
 681 is not clear whether it is due to the lift-response function or to the definition of the stagger angle,
 682 which is a sensitive parameter for the upstream results as alluded before. Recall that PropNoise
 683 uses the leading-edge angle and TinA1D the mean flow angle to define the inclination of the plate
 684 (see Tab. A1).
- 685 • *Free-field Isolated Airfoil*: The comparison between PN2 and OB1 allows to further compare Sears
 686 and Amiet. One additional difference is that, unlike PN2, OB1 works with the two-dimensional
 687 wavenumber spectrum. The two results are in good agreement for all simulations in both
 688 directions of propagation. The discrepancy does not exceed 3 dB.
- 689 • *Isolated Airfoil vs. Cascade of Airfoils*: As the solidity (chord-to-pitch ratio) grows, the cascade
 690 effect is expected to have an increasing impact on noise. In the ACAT1 case, the stator solidity
 691 varies between 2.5 at the hub and 1.4 at the tip (see Fig. 7). Hanson [6], using a three-dimensional
 692 cascade-response model, found little impact on his results, even at low frequency, when he varied
 693 the solidity in the range 0.8 to 2.5, while keeping the blade count constant. These findings are
 694 not in agreement with Grace's results [59] for a shrouded configuration. Indeed, she observed
 695 differences superior to 5 dB at high frequency on the baseline configuration of the SDT fan but
 696 comparable levels at low frequency. The same conclusion can be drawn from de Laborderie's
 697 results [26] for the same fan. Thus, published results show contrary trends between open and
 698 ducted configurations. The reason for this is not yet understood.

Comparing the single airfoil model to the cascade model in 2D, Blandeau et al. [22] reported potentially severe differences between the two solutions at frequencies below a critical value. Above that critical frequency, blade-to-blade interactions are weak and the contribution of all blades to the radiated sound power are additive. Below the critical limit, the results are worse. By neglecting the cascade effect, the results become increasingly unsuitable as the solidity augments. In their examples, a good match was found for a value of solidity below one. For a 2D cascade, the critical frequency [50] is given by:

$$f_c = \frac{1 - M^2}{M_t + \sqrt{1 - M_x^2}} \frac{c_0}{s}, \quad (27)$$

699 where M_x and M_t are the axial and tangential Mach numbers, $M = \sqrt{M_x^2 + M_t^2}$, and s is the pitch.
 700 At the Approach condition, the following values are found in the benchmark data at midspan:
 701 $M_x \approx 0.33$, $M_t \approx 0.21$, $c_0 \approx 343$ m/s and $s \approx 4.85 \times 10^{-2}$ m. This yields as critical frequency
 702 $f_c \approx 4,600$ Hz. A convergence at high frequency, starting in a frequency range not too far from
 703 that predicted by Cheong et al. is observed between OB1 (single airfoil) and OB2 (3D cascade).
 704 The solution OB3 (3D cascade) also converges to the isolated case but at a much higher frequency.
 705 A reduction of the noise levels in the low-frequency range is observable for the OB2, OB3, LN1 and

LN2 simulations but not for the LN3 and OP1 curves. The LN3 solution is 2D, which produces the difference as already explained. Concerning OP1, no strong reduction of the noise levels in the low-frequency range is observed because the number of CAA calculations used to derive the *a priori* correction of the turbulence content were not enough. Only a small amount of CAA simulations were performed and it seems that those were sufficient to reproduce the results at high frequency but insufficient to better account for the low-frequency behaviour. Also note that the TA2 results, which do not consider the cascade effect but do account for the oblique gusts, are very similar to OB2. Thus, it is not clear whether the effect of oblique gusts is dominant over the cascade effect.

- *Cascade of Flat Plates vs. Cascade of Thick, Cambered Airfoils*: The comparison between BB1 and LN1 at the condition Approach indicates that considering the real blade geometry does not significantly modify the results. Using a solution valid upstream of the cascade, Evers and Peake [58] also found that considering thickness and camber has a relatively small impact on broadband noise, which is no longer true for tonal noise. Grace [59], using the asymptotic solution for an isolated single blade provided by Ayton and Peake [60], investigated the effect of thickness, camber and angle of attack. For a realistic choice of parameters, the differences reported by Grace did not exceed 3 dB. Using a synthetic turbulence method coupled to a CAA solver, Gea-Aguilera et al. [61] found similar results for fan RSI noise.

5. Conclusion

A benchmark concerning RANS-informed analytical methods applied to rotor–stator interaction broadband noise of turbofan was organised within the framework of the European project TurboNoiseBB. The objective was twofold: i) to analyse the impact of the Reynolds-Averaged Navier-Stokes calculation on the intermediate turbulence statistics and the final acoustic prediction, ii) to quantify and assess the influence of the acoustic models. The first question was addressed in the companion paper [1] considering various turbulence models while the same acoustic code was used to make the noise prediction. For this second part, an inverse strategy was applied: the acoustic models were varied while the same RANS solutions were used as input.

The experimental data of the benchmark were obtained for the transonic fan ACAT1 of AneCom AeroTest. The benchmark made use of the data recorded at the three operating conditions, Approach, Cutback and Sideline along the sea level static working line.

The acoustic tools of the benchmark have differing application objectives and therefore do not need the same accuracy. This explains the very broad range of measured computation time: between one minute and more than one day per acoustic simulation. A classification of the models in two categories was initiated. Group A contained methods based on the acoustic analogy and Group B, the direct acoustic methods bypassing the calculation of a source term. Regarding methods of type A, the following issues were identified: 1) a mismatch between the source model and the Green’s function (swirl was considered either with a simplified model or not at all), 2) significant variations of the power radiation with the choice of the stagger angle, 3) an uncertainty regarding the consideration of the oblique, spanwise gust component in results using a 2D cascade unsteady lift response. Methods of type B exhibited the following issues: 1) a noise overestimation, in particular at low frequency, for the methods based on a 2D acoustic cascade response because spanwise variations of the gust cannot be considered, 2) no straightforward solution to account for the annular duct, which should mostly impact the low frequency behaviour too.

A direct comparison of the acoustic results was difficult as oftentimes models differed from each other in more than one aspect. Nevertheless, the benchmarking activity on the fan ACAT1 led to the following findings:

- Similarly to the RANS turbulence model, the chosen approach to model acoustics may have a significant impact on the predictions of RSI broadband noise. At frequencies higher than the peak frequency, differences of up to ± 3 dB were observed between the results and the median

755 solution. At lower frequencies, the deviation was even more substantial, mainly for two reasons:
756 the presence of subcritical gusts and the cutoff effect of acoustic modes, which are both important
757 to consider when the number of contributing waves is small.

- 758 • Compared to experiments, the predicted levels were usually lower by some decibels, even though
759 the turbulence intensity was overestimated by the RANS simulations.
- 760 • The choice of the turbulence spectrum (whether Liepmann or von Kármán) was not of primary
761 importance for the results.
- 762 • Concerning the Green's function, an impact was observed at low frequency between the open
763 and induct solutions. The difference was smaller by applying the isolated airfoil solution than by
764 considering the cascade effect.
- 765 • For the case investigated at the lowest Mach number, it could be shown that replacing the real
766 blade geometry by a flat plate is an acceptable assumption for broadband noise. This is likely
767 totally different for tonal noise predictions as the chordwise distribution of the pressure jump is
768 known to be different for real airfoils.
- 769 • The trends predicted by increasing the rotor speed were similar for almost all models. They were
770 principally driven by the changes in the velocity turbulence spectrum.
- 771 • Two-dimensional cascade-based models have inherent difficulties to account for the third, i.e.
772 the spanwise, dimension. Several solutions were developed by the participants to overcome that
773 problem. Without these corrections, broadband noise is overestimated at low frequency. With
774 this respect, the single airfoil theory considering the oblique component produces better results.
- 775 • The split between the up- and downstream power levels exhibited different trends for the
776 single-airfoil and the cascade results.

777 It was not possible to determine the best combination of models in terms of accuracy because
778 of the uncertainties regarding i) the turbulence statistics issued from the RANS calculations used to
779 feed the acoustic models, and ii) the acoustic validation data, as these included the contribution of all
780 acoustic sources in the test rig and not solely rotor–stator interaction noise.

781 All the benchmark participants considered the turbulence as being isotropic. However, the
782 hot-wire measurements in the interstage indicate that this assumption is increasingly unsuitable
783 with an increasing proximity to the casing wall due the rotor tip vortex and the boundary layer.
784 Reconsidering the way the turbulence is modelled - at least in the regions near the walls - could be
785 necessary to achieve more accurate predictions.

786 Since one of the principal objectives of RANS-informed analytical methods for fan noise is to
787 properly predict acoustic trends, it would be necessary to conduct an additional benchmark treating
788 a more complex vane geometry. Certain model features, which are seemingly negligible for the
789 investigated case, may be essential for such cases.

790 **Author Contributions:** Conceptualization, S.G. and C.K.; methodology, S.G. and C.K.; software, all; validation,
791 all; formal analysis, S.G., P.S. and C.K.; investigation, S.G., C.K. and P.S.; resources, all; data curation, S.G., P.S.
792 and C.K.; writing–original draft preparation, S.G.; writing–review and editing, all; visualization, S.G. and P.S.;
793 supervision, S.G. and C.K. All authors have read and agreed to the published version of the manuscript.

794 **Funding:** This work was conducted in the frame of the project TurboNoiseBB, which has received funding from
795 the European Union's Horizon 2020 research and innovation programme under grant agreement No. 690714.

796 **Acknowledgments:** The authors would like to gratefully acknowledge the support of following people: Azucena
797 Pintado and Thomas Nodé-Langlois (AIRBUS), Marc Jacob and Stéphane Moreau (ECL), Maximilian Behn and
798 Sebastian Hakansson (DLR), Phil Joseph (ISVR), and Adolfo Serrano (ITP Aero).

799 **Conflicts of Interest:** The authors declare no conflict of interest.

800 **Abbreviations**

801 The following abbreviations are used in this manuscript:

| | |
|----------|---|
| ACAT1 | AneCom AeroTest Rotor 1 |
| AP | Approach |
| BPF | Blade Passing Frequency |
| CAA | Computational AeroAcoustics |
| CB | Cutback |
| CFD | Computational Fluid Dynamics |
| ESS | Engine Support Stator |
| HW | Hot Wire (anemometry) |
| LE | Leading edge |
| NASA | National Aeronautics and Space Administration |
| PWL | Sound Power Level |
| 802 RANS | Reynolds Averaged Navier-Stokes |
| rpm | round per minute |
| RSI | Rotor–Stator Interaction |
| SDT | Source Diagnostic Test (fan rig) |
| SL | Sideline |
| SLS | Sea Level Static (working line) |
| TE | Trailing edge |
| TKE | Turbulence Kinetic Energy |
| TLS | Turbulence Length Scale |
| TNBB | EU founded project TurboNoiseBB |
| UFFA | Universal Fan Facility for Acoustics |

803 Appendix A Summary of the acoustic models

| Code | ID | turbulence spectrum | blade model | gust | acoustic conditions | |
|----------------------|----------|---------------------|--|----------|----------------------------------|-------------------------------|
| | | | | | mean flow | boundaries |
| PropNoise [40,41] | PN1 | v. Kármán | isolated flat plate with χ_A [8] | parallel | axial uniform + solid body swirl | infinite duct with hard walls |
| | PN2 | | | | axial uniform | free field |
| OPTIBRUI [26] | OB1 [48] | Liepmann | isolated flat plate with χ_A [8] | oblique | axial uniform | free field |
| | OB2 [6] | | cascade of flat plates with χ_A [11] | | stripwise swirling flow | |
| | OB3 [24] | | | | axial uniform | infinite duct with hard walls |
| BBNANEMS | BB1 [54] | Liepmann | cascade of real blades [55] | parallel | stripwise swirling flow | free field |
| | LN1 [53] | | cascade of flat plates with χ_A [51] | | | |
| | LN2 | | cascade of flat plates with χ_A [13,51] | oblique | | |
| TinA [44,45] | TA1 | v. Kármán | isolated flat plate with β_A [8] | parallel | axial uniform | infinite duct with hard walls |
| | TA2 | | | oblique | | |
| Orpheus [57] | OP1 | Liepmann | cascade of flat plates with χ_A [51] | oblique | axial uniform strip based | infinite duct with hard walls |
| LINSUB | LN3 [50] | Liepmann | cascade of flat plates with χ_A [51] | parallel | stripwise swirling flow | free field |

Table A1. Characteristics of the acoustic models and principal references.

| ID | number of strips | number of frequencies | rough estimate of the computation time |
|-----|------------------|-----------------------|--|
| PN1 | 97 | 100 | 1 min |
| PN2 | 97 | 100 | 1 min |
| OB1 | 25 | 25 | 1 min |
| OB2 | 25 | 25 | 3 hr on 24 cores |
| OB3 | 25 | 25 | 2 hr on 240 cores |
| BB1 | 5 | 39 | 170 GPU hr / 8500 CPU hr |
| LN1 | 5 | 39 | 2 min |
| LN2 | 5 | 39 | 10 min |
| TA1 | 97 | 24 | 1 min |
| TA2 | 10 | 24 | 1 hr |
| OP1 | 9 | 315 | 25 min |
| LN3 | 49 | 100 | 8 hr |

Table A2. Simulation parameters.

804 Appendix B Modal sound power amplitude

A time-harmonic variation such as $p(\mathbf{x}, t) = \hat{p}(\mathbf{x}, \omega)e^{-i\omega t}$ is considered. In mean swirling flows with a constant axial velocity (Mach number: M_x) and a small solid-body rotation at angular velocity Ω_s , the pressure field can be decomposed into a sum of orthogonal eigenmodes of azimuthal and radial orders m and n :

$$p(\mathbf{x}, \omega) = \sum_{m,n} A_{mn}^{\pm} e^{ik_{x,mn}^{\pm} x} e^{im\theta} f_{mn}(r). \quad (\text{A1})$$

The function f_{mn} describes the radial variation of the pressure of the mode. Its solution is obtained by solving a second-order ordinary differential equation on the pressure. In annular ducts, the function f_{mn} is composed of a sum of Bessel (J_m) and Newmann (Y_m) functions of order m [62]:

$$f_{mn}(r) = \frac{1}{\sqrt{F_{mn}}} \left[J_m \left(\sigma_{mn} \frac{r}{R} \right) + Q_{mn} Y_m \left(\sigma_{mn} \frac{r}{R} \right) \right], \quad (\text{A2})$$

with

$$Q_{mn} = -\frac{J'_m(\sigma_{mn})}{Y'_m(\sigma_{mn})}. \quad (\text{A3})$$

The symbol " ' " denotes radial derivatives. The function f_{mn} is normalised with F_{mn} such as

$$\frac{1}{2\pi R^2} \int_0^{2\pi} \int_{\eta R}^R |f_{mn}(r)|^2 r dr d\theta = 1. \quad (\text{A4})$$

For hard walls, the factor σ_{mn} is defined so that the equality

$$f'_{mn}(r)|_{r=\eta R, R} = 0 \quad (\text{A5})$$

is satisfied at the hub and casing walls. The axial wavenumber $k_{x,mn}^{\pm}$ and the cut-off factor α_m are defined as follows:

$$k_{x,mn}^{\pm} = \frac{k\delta_m}{1 - M_x^2} (-M_x \pm \alpha_m), \quad (\text{A6})$$

$$\alpha_m = \sqrt{1 - \frac{(1 - M_x^2) \sigma_{mn}^2}{\delta_m^2 (kR)^2}}. \quad (\text{A7})$$

The swirl factor δ_m ,

$$\delta_m = 1 - \frac{mM_s}{kR}, \quad (\text{A8})$$

accounts for the presence of the rigid body swirl [63]. The swirl Mach number $M_s = \Omega_s R / c_0$ is calculated at the tip wall. It should satisfy $M_s \ll 1$. The modal sound power is given by

$$P_{mn}^{\pm} = \pi R^2 \frac{\alpha_{mn}}{\rho_0 c_0 \delta_m} C_{mn}^{\pm} |A_{mn}^{\pm}|^2, \quad (\text{A9})$$

with

$$C_{mn}^{\pm} = \frac{(1 - M_x^2)^2}{(1 \mp \alpha_{mn} M_x)^2}. \quad (\text{A10})$$

Notice that in the current derivation A_{mn} is a peak amplitude, whereas A_{mn} corresponds to a root-mean square value in Eq. (5). As a consequence the modal sound power in Eq. (A9) has to be multiplied by a factor 2 when applied to broadband noise. The sound power spectrum P^{\pm} is obtained by summing the contributions of all cut-on modes at the same frequency:

$$P^{\pm}(\omega) = \sum_{m,n} P_{mn}^{\pm}(\omega). \quad (\text{A11})$$

805

806 References

- 807 1. Kissner, C.; Gu erin, S.; Seeler, P.; Billson, M.; Paruchuri, C.; P. C. Lara na; de Laborderie, H.; Fran ois B.,
808 Lefarth, K.; Lewis, D.; Villar, G. M.; Nod e-Langlois. ACAT1 benchmark of RANS-informed analytical
809 methods for fan noise prediction: Part I - Influence of the RANS Simulation. Submitted to *Acoustics* 2020.
- 810 2. Rienstra, S. Sound transmission in slowly varying circular and annular lined ducts with flow ducts, *J. Fluid*
811 *Mech.* **1999**, 380; pp. 279–296.
- 812 3. Ribner, H. S. Shock-turbulence interaction and the generation of noise. NACA Report TR-1233, 1954.
- 813 4. Posson, H.; Roger, M.; Moreau, S. On a uniformly valid analytical rectilinear cascade response function. *J.*
814 *Fluid Mech.* **2010**, 663; pp. 22–52.
- 815 5. Amiet, R. Acoustic radiation from an airfoil in a turbulent stream. *J. Sound Vib.* **1975**, 41(4); pp. 407–420.
- 816 6. Hanson, D. Theory for Broadband Noise of Rotor and Stator Cascades with Inhomogeneous Inflow
817 Turbulence Including Effects of Lean and Sweep. NASA CR-2001-210762, 2001.
- 818 7. Curle, N. The influence of solid boundaries upon aerodynamic sound. *Proc. Royal Soc.* **1955**, A231; pp.
819 505–514.
- 820 8. Amiet, R. Compressibility effects in unsteady thin-airfoil theory. *AIAA J.* **1974**, 12(2); pp. 252–254.
- 821 9. Sears, W. Some aspects of non-stationary airfoil theory and its practical applications. *J. Aeronaut. Sci.* **1941**,
822 8(3); pp. 104–108.
- 823 10. Adamczyk, J.J. The passage of an infinite swept airfoil through an oblique gust. NASA CR-2395, 1974.
- 824 11. Glegg, S. The response of a swept blade row to a three-dimensional gust. *J. Sound Vib.* **1999**, 227(1); pp.
825 29–64.
- 826 12. Goldstein, M. *Aeroacoustics*; McGraw-Hill, 1976.
- 827 13. Graham, J. Similarity rules for thin aerofoils in non-stationary subsonic flows. *J. Fluid Mech.* **1970**, 43(4); pp.
828 753–766.
- 829 14. Kerschen, E.; Gliebe, P. Fan Noise Caused by Ingestion of Anisotropic Turbulence - A Model Based on
830 Axisymmetric Turbulence Theory. In Proceedings of the 6th AIAA Aeroacoustics Conference, AIAA-80-1021,
831 Hartford (CT), USA, 4-6 June 1980.
- 832 15. Ventres, C.; Theobald, M.; Mark, W. Turbofan Noise Generation, Volume 1: Analysis. NASA CR-167952,
833 1982.
- 834 16. Nallasamy, M.; Envia, E. Computation of rotor wake turbulence noise. *J. Sound Vib.* **2005**, 282; pp 649–678.
- 835 17. Grace, S.; Wixom, A.; Winkler, J.; Sondak, D.; Logue, M. M. Fan Broadband Interaction Noise Modeling 2012.
836 In Proceedings of the 18th AIAA/CEAS Aeroacoustics Conference, AIAA-2012-2269, Colorado Springs (CO),
837 USA, 4-6 June 2012.
- 838 18. Kissner, C.A.; Gu erin, S. Influence of Wake and Background Turbulence on Predicted Fan Broadband Noise.
839 *AIAA J.* 2019, 58(2).

- 840 19. Grace, S.; Maunus, J.; Sondak, D. Effect of CFD Wake Prediction in a Hybrid Simulation of Fan Broadband
841 Interaction Noise. In Proceedings of the 17th AIAA/CEAS Aeroacoustics Conference, AIAA-2011-2875,
842 Portland (OR), USA, 5-8 June 2011.
- 843 20. Moreau, A.; Guérin, S. The impact of low-speed fan design on noise: an exploratory study. *J. Turboma.* **2016**,
844 *138*.
- 845 21. Jaron, R.; Herthum, H.; Franke, M.; Moreau, A.; Guérin, S. Impact of turbulence models on RANS-informed
846 prediction of fan broadband noise. In Proceedings of 12th European Conference on Turbomachinery Fluid
847 dynamics and Thermodynamics, ETC2017-067, Stockholm, Sweden, 3-7 April 2017.
- 848 22. Blandeau, V.P.; Joseph P.F.; Jenkins G.; Powles C.J. Comparison of sound power radiation from isolated
849 airfoils and cascades in a turbulent flow. *J Acoust. Soc. Am.* **2011**, *129(6)*; pp. 3521-3530.
- 850 23. Grace, S. Fan broadband interaction noise modeling using a low-order method. *J. Sound Vib.* **2015**, *346*; pp.
851 402–423.
- 852 24. Posson, H.; Moreau, S.; Roger, M. Broadband noise prediction of fan outlet guide vane using a cascade
853 response function. *J. Sound Vib.* **2011**, *330*; pp. 6153–6183.
- 854 25. Posson, H.; Moreau, S.; Roger, M. On the use of a uniformly valid analytical cascade response function for
855 fan broadband noise predictions. *J. Sound Vib.* **2011**, *329*; pp. 3721-3743.
- 856 26. de Laborderie, J. Approches analytiques et numériques pour la prédiction du bruit tonal et large bande de
857 soufflantes de turboréacteurs. Thèse de doctorat, Université de Sherbrooke (Canada), 2013.
- 858 27. Lewis, D.; Moreau, S.; Jacob, M. On the use of RANS-informed analytical models to perform broadband
859 rotor-stator interaction noise predictions. In Proceedings of the 25th AIAA/CEAS Aeroacoustics Conference,
860 AIAA-2019-2667, Delfs, The Netherlands, 20-23 May 2019.
- 861 28. TurboNoiseBB, European Union's Horizon 2020 research and innovation programme. [http://dlr.de/at/
862 turbonoisebb](http://dlr.de/at/turbonoisebb), last accessed: 2020-05-09.
- 863 29. Guérin, S.; Kissner, C.; Kajasa, B.; Jaron, R.; Behn, M.; Hakansson, S.; Pardowitz, B.; Tapken, U.; Meyer, R.;
864 Enghardt, L. Noise prediction of the ACAT1 fan with a RANS-informed analytical method: success and
865 challenge. In Proceedings of the 25th AIAA/CEAS Aeroacoustics Conference, AIAA-2019-2500, Delfs, The
866 Netherlands, 20-23 May 2019.
- 867 30. Meyer, R.; Hakansson, S.; Hage, W.; Enghardt, L. Instantaneous flow field measurements in the interstage
868 section between a fan and the outlet guiding vanes at different axial positions. In Proceedings of the 13th
869 European Conference on Turbomachinery Fluid Dynamics and Thermodynamics, ETC2019-330, Lausanne,
870 Switzerland, 8-12 April 2019.
- 871 31. Tapken, U.; Behn, M.; Spitalny, M.; Pardowitz, B. Radial mode breakdown of the ACAT1 fan broadband
872 noise generation in the bypass duct using a sparse sensor array. In Proceedings of the 25th AIAA/CEAS
873 Aeroacoustics Conference, AIAA-2019-2400, Delfs, The Netherlands, 20-23 May 2019.
- 874 32. Tapken, U.; Pardowitz, B.; Behn, M. Radial mode analysis of fan broadband noise. In Proceedings of the 23rd
875 AIAA/CEAS Aeroacoustics Conference, AIAA-2017-3715, Denver (CO), USA, 5-9 June 2017.
- 876 33. Behn, M.; Pardowitz, B.; Tapken, U. Separation of tonal and broadband noise components by cyclostationary
877 analysis of the modal sound field in a low-speed fan test rig. In Proceedings of fan2018, Darmstadt, Germany,
878 18-20 April 2018.
- 879 34. Joseph, P.; Morfey, C.; Lowis, C. Multi-mode sound transmission in ducts with flow. *J. Sound Vib.* **2003**, *264*;
880 pp. 523–544.
- 881 35. Pereira, A.; Jacob, M. Experimental assesement of in-duct modal content of fan broadband noise via
882 iterative Bayesian inverse approach. In Proceedings of Berlin Beamforming Conference, Berlin, Germany,
883 BeBeC-2020-D20.
- 884 36. Becker, K.; Heitkamp, K.; Kügeler, E. Recent Progress in a Hybrid Grid CFD Solver for Turbomachinery
885 Flows. In Proceedings of the Fifth European Conference on Computational Fluid Dynamics, ECCOMAS
886 CFD 2010, Lisbon, Portugal, 14-17 June 2010.
- 887 37. Menter, F.R. Two-equation eddy-viscosity turbulence models for engineering applications. *AIAA J.* **1994**, *32*;
888 pp. 1598–1605.
- 889 38. Pope, S. *Turbulent flows*; Cambridge University Press, 2011.
- 890 39. Jaron, R. Aeroakustische Auslegung von Triebwerksfans mittels multidisziplinärer Optimierungen.
891 Dissertation, Technische Universität Berlin, 2018.

- 892 40. Moreau, A. A unified analytical approach for the acoustic conceptual design of fans of modern aero-engines.
893 Dissertation, Technische Universität Berlin, 2017.
- 894 41. Moreau, A.; Guérin, S. Similarities of the in-duct and free-field formulations in rotor noise problems. In
895 Proceedings of the 17th AIAA/CEAS Aeroacoustics Conference, AIAA-2011-2759, Portland (OR), USA, "5-8
896 June 2011.
- 897 42. Hanson, D. B. Helicoidal surface theory for harmonic noise of propellers in the far field. *AIAA J.* **1980**, *18*(10);
898 pp 1213–1220.
- 899 43. Blokhinstev, D. The propagation of sound in an inhomogeneous and moving medium. *J Acoust. Soc. Am.*
900 **1946**, *18*; pp. 322–328.
- 901 44. Reboul, G.; Polacsek, C.; Léwy, S.; Heib, S. Ducted-Fan Broadband Noise Simulations Using Unsteady or
902 Averaged Data. In Proceedings of inter.noise 2008 - 37th International Congress and Exposition on Noise
903 Control Engineering, Shanghai, China, 26-29 October, 2008.
- 904 45. Reboul, G. Modélisation du bruit à large bande de soufflante de turboréacteur. Thèse de doctorat de l'Ecole
905 Centrale de Lyon (France), 2010
- 906 46. Amiet, R. High-frequency thin-airfoil theory for subsonic flow. *AIAA J.* **1976**, *14*(8); pp. 1076–1082.
- 907 47. Guérin, S.; Moreau, A.; Tapken, U. Relation between source models and acoustic duct modes. In Proceedings
908 of the 15th AIAA/CEAS Aeroacoustics Conference, AIAA-2009-3364, Miami (FL), USA, 11-13 May 2009.
- 909 48. Amiet, R.; Egolf, C.; Simonich, J. Noise produced by turbulent flow into a rotor: users manual for noise
910 calculation. NASA CR-181790, 1989.
- 911 49. Hanson, D.; Horan, K. Turbulence/cascade interaction, spectra of inflow, cascade response, and noise. In
912 Proceedings of the AIAA/CEAS Aeroacoustics Conference, AIAA-98-2319, Toulouse (France), 2-4 June 1998.
- 913 50. Cheong, C.; Joseph, P.; Lee, S. High frequency formulation for the acoustic power spectrum due to
914 cascade-turbulence interaction. *J. Acoust. Soc. Am.* **2006**, *119*(1); pp. 108–122.
- 915 51. Whitehead, D. AGARD Manual on Aeroelasticity in Axial-Flow Turbomachines, Volume 1, Unsteady
916 Turbomachinery Aerodynamics, Classical two-dimensional methods. AGARD-AG-298, 1987.
- 917 52. Smith, S.N. Discrete frequency sound generation in axial flow turbomachines. Aeronautical Research Council
918 Reports and Memoranda, Reports and Memoranda No. 3709, 1970.
- 919 53. Blázquez, R.; Corral, R. Efficient Fan Broadband Noise Prediction using Navier-Stokes Linearized Analysis.
920 In Proceedings of the 25th AIAA/CEAS Aeroacoustics Conference, AIAA-2019-2624, Delfs, The Netherlands,
921 20-23 May 2019.
- 922 54. Blázquez, R.; Corral, R. Prediction of fan acoustic blockage on fan-outlet guide vanes broadband
923 interaction noise. In Proceeding of the 15th Turbomachinery Technical Conference and Exposition GT2020,
924 GT2020-15574, London, UK, 22-26 June 2020.
- 925 55. Corral, R.; Escribano, A.; Gisbert, F.; Serrano, A.; Vasco, C. Validation of a linear multigrid accelerated un
926 structured Navier-Stokes solver for the computation of turbine blades on hybrid grids. In Proceedings of the
927 9th AIAA/CEAS Aeroacoustics Conference, AIAA-2003-3326, Hilton Head (SC), USA, 12-14 May 2003.
- 928 56. Wohlbrandt, A.; Kissner, C.; Guérin, S. Impact of cyclostationarity on fan broadband noise prediction. *J.*
929 *Sound Vib.* **2018**, *420*, pp. 142–164.
- 930 57. Carrasco Laraña, P. C.; Serrano, A. A Frequency Domain Model for Turbine Interaction Broadband Noise:
931 Comparison with Measurements. In Proceedings of the 24th AIAA/CEAS Aeroacoustics Conference,
932 AIAA-2018-3917, Atlanta (GA), USA, 25-29 June 2018.
- 933 58. Evers I.; Peake N. On sound generation by the interaction between turbulence and a cascade of airfoils with
934 non-uniform mean flow. *J. Fluid Mech.* **2002**, *463*, pp. 25–52.
- 935 59. Grace, S. Further Investigations Into a Low-Order Model of Fan Broadband Noise. In Proceedings of the 21st
936 AIAA/CEAS Aeroacoustics Conference, AIAA-2015-3283, Dallas (TX), USA, 22-26 June 2015.
- 937 60. Ayton, L.J.; Peake, N. On high-frequency noise scattering by aerofoils in Flow. *J. Fluid Mech.* **2013**, *734*; pp.
938 144–182.
- 939 61. Gea-Aguilera, F.; Gill, J.; Zhang, X. On the effects of fan wake modelling and vane design on cascade noise. *J.*
940 *Sound Vib.* **2019**, *459*.
- 941 62. Morse, M.; Ingard, K. *Theoretical acoustics*; Princeton (reprinted), 1986.
- 942 63. Morfey, C. Sound transmission and generation in ducts with flow. *J Sound Vib.* **1971**, *14*(1); pp. 37–55.

943 © 2020 by the authors. Submitted to *Acoustics* for possible open access publication under the terms and conditions
944 of the Creative Commons Attribution (CC BY) license (<http://creativecommons.org/licenses/by/4.0/>).